



Flexural wave band gaps in a multi-resonator elastic metamaterial plate using Kirchhoff-Love theory

E.J.P. Miranda Jr. ^{a,*}, E.D. Nobrega ^{b,c}, A.H.R. Ferreira ^b, J.M.C. Dos Santos ^b

^a Federal Institute of Maranhão, IFMA-EIB-DE, Rua Afonso Pena, 174, CEP 65010-030 São Luís, MA, Brazil

^b University of Campinas, UNICAMP-FEM-DMC, Rua Mendeleyev, 200, CEP 13083-970 Campinas, SP, Brazil

^c Federal University of Maranhão, UFMA-CCET-CCEM, Avenida dos Portugueses, 1966, CEP 65080-805 São Luís, MA, Brazil

ARTICLE INFO

Article history:

Received 30 September 2017

Received in revised form 2 June 2018

Accepted 28 June 2018

Keywords:

Elastic metamaterial thin plate

Flexural wave band gaps

Multiple degrees of freedom

3D printing

Vibration control

ABSTRACT

We investigate theoretically the band structure of flexural waves propagating in an elastic metamaterial thin plate. Kirchhoff-Love thin plate theory is considered. We study the influence of periodic arrays of multiple degrees of freedom local resonators in square and triangular lattices. Plane wave expansion and extended plane wave expansion methods, also known as $\omega(\mathbf{k})$ and $\mathbf{k}(\omega)$, respectively, are used to solve the governing equation of motion for a thin plate. The locally resonant band gaps for square and triangular lattices present almost the same attenuation for all examples analysed. However, square lattice presents broader Bragg-type band gaps with higher attenuation than triangular lattice. An experimental analysis is conducted with a real elastic metamaterial thin plate with resonators in a square lattice. Modal analysis and forced response are computed by finite element method. Plane wave expansion, finite element and experimental results present good agreement.

© 2018 Elsevier Ltd. All rights reserved.

1. Introduction

Over the last decades artificial composites known as phononic crystals (PCs) consisting of scatterer (inclusion) periodic arrays embedded in a host medium (matrix) have been well studied [1–18]. They have received renewed attention because they exhibit band gaps where there are no mechanical (elastic or acoustic) propagating waves, only evanescent waves. The physical origin of phononic and photonic band gaps can be understood at the micro-scale using the classical wave theory to describe Bragg and Mie resonances based on the scattering of mechanical and electromagnetic waves propagating within the crystal [19].

In PC investigation, band gap formation is based on the Bragg scattering mechanism, whose frequency location is governed by Bragg's law, $a = n(\lambda/2)$, ($n \in \mathbb{N}_{>0}$), where a is the lattice parameter of the periodic system and λ is the wavelength in the host material. Bragg's law implies that it is difficult to achieve a low-frequency Bragg-type band gap for small size PCs. Difficulties to design PCs with low frequency band gaps for small sizes instigated researchers to explore other dissipative mechanisms together with the effect of periodicity. In 2000, Liu and co-workers [20] proposed a locally resonant PC, also known as elastic metamaterial (EM), containing an array of localized resonant structures. Resonance-type band gaps were obtained in a frequency range two orders of magnitude lower than that given by the Bragg's limit. Locally resonant band gaps

* Corresponding author.

E-mail address: edson.jansen@ifma.edu.br (E.J.P. Miranda Jr.).

arise on the vicinity of the natural frequency of the resonator while Bragg-type band gaps typically occur at wavelengths of the order of unit cell size.

EMs have been proposed for instance as acoustic barriers [21,22], vibration isolators [23–27] and noise suppression devices [28,29] with emphasis on low frequency applications. There are various types of elastic structures being investigated containing an array of resonators, such as rods [30–32], beams [33–46], plates [47–56,46] and shells [57]. These local resonators can be modelled by spring-mass resonators of single degree of freedom (S-DOF) [30,33,34,36–38,41,42,47–50,53,57,55,51,46] or multiple degrees of freedom (M-DOF) [31,32,35,39,40,43–45,52,58,59,56].

Torrent and co-workers [51] studied an EM thin plate system consisting of a honeycomb arrangement of attached spring-mass resonators. From the band structure calculation, they showed the presence of Dirac points near the K point of the Brillouin zone. The presence of edge states was studied using multiple scattering theory. Haslinger et al. [56] investigated semi-infinite periodic systems of point resonators and discussed the association with the infinite systems for square and rectangular lattices. An alternative approach using Green's functions and multipole methods to obtain dispersion diagrams for S-DOF and M-DOF structured plates was employed. Pal and Ruzzene [55] studied EMs characterized by topologically non-trivial band gaps supporting backscattering suppressed edge waves. These edge waves are topologically protected and are obtained by breaking inversion symmetry within the unit cell. They considered an EM plate containing a honeycomb arrangement of resonators. The S-DOF array of resonators generates a Dirac cone whose properties may be altered by breaking inversion symmetry through introducing alternating mass values in the unit cell.

Since periodic resonator-type structures started recently to be investigated in many engineering applications for vibration control [60,61], the main purpose of this paper is to investigate the elastic band structure, also known as dispersion diagram, of flexural waves propagating in an EM thin plate with attached multiple resonators of M-DOF in the unit cell, considering square and triangular lattices. Kirchhoff-Love plate theory [62,63] is applied for thin plate modelling. Plane wave expansion (PWE) [1,2] and extended plane wave expansion (EPWE) [64–70] methods, also known as $\omega(\mathbf{k})$ and $\mathbf{k}(\omega)$, respectively, are used to predict the complex band structure of the EM thin plate.

By using a real EM thin plate an experimental test is performed. An EM thin plate with square lattice is manufactured with a polymer (Vero White Plus) in a 3D printer with UV curing technology. Simulated results with finite element (FE) method, *i.e.* frequency response function (FRF), and with PWE method, *i.e.* band structure, are compared to the experimental data. Some different behaviours and mismatches between simulated and experimental results are found. These differences are reduced after a trial-and-error model updating by varying material property parameters (Young's modulus and mass density). PWE formulated can localize band gap position and width close to the experimental and FE results.

The paper is organized as follows. Section 2 presents PWE and EPWE approaches for an EM thin plate with periodic arrays of attached M-DOF resonators based on Kirchhoff-Love plate theory [62,63]. In the following, *i.e.* Section 3, simulated examples are carried out considering some test cases: (I) single resonator of S-DOF, (II) multiple resonators of S-DOF, (III) single resonator of M-DOF and (IV) multiple resonators of M-DOF. In Section 4 an experimental validation of EM thin plate and simulated verification using FE and PWE are performed. Conclusions are presented in Section 5. Appendices A and B present some mathematical manipulations for PWE and EPWE approaches.

2. Elastic metamaterial thin plate modelling

This section presents the formulation for an EM thin plate using PWE and EPWE methods based on Kirchhoff-Love plate theory. We consider two-dimensional periodicity, *i.e.* 2D PC, isotropic elastic plate and wave propagation in the xy plane.

PWE and EPWE are semi-analytical methods used to predict the band structure of PCs and EMs. The advantage of using EPWE over PWE is that evanescent modes are obtained naturally and they are not ignored as with PWE method. PWE assumes that Bloch wave vector, *i.e.* \mathbf{k} , also known as wave number, is real. In addition, EPWE method is not restricted to the first Brillouin [71] zone (FBZ) [67]. Hsue and co-workers [66] proved that the evanescent modes obtained by EPWE obey Floquet-Bloch's theorem [72,73].

Some recent studies have been developed on EM modelling using PWE and EPWE methods. Xiao and co-workers proposed PWE and EPWE methods to model a metamaterial Euler-Bernoulli beam [37] and a metamaterial Kirchhoff-Love [62,63] plate [49] with attached resonators of S-DOF in the unit cell. Moreover, Torrent and co-workers [51] used the PWE method to study an EM thin plate with attached S-DOF resonators, considering honeycomb lattice. Here, we expand the formulation of Xiao et al. [49] for an EM thin plate with attached multiple resonators of M-DOF in the unit cell, considering square and triangular lattices.

Fig. 1 sketches an infinite EM thin plate with attached single resonator of M-DOF in the unit cell, considering square (a) and triangular (b) lattices. Fig. 1 (a – b) also represents the first irreducible Brillouin zone (FIBZ) [71] in shaded region for square and triangular lattices, respectively. The FIBZ points in Fig. 1 (a – b) are Γ (0, 0), X (π/a , 0) and M (π/a , π/a) for square lattice and Γ (0, 0), X ($4\pi/3a$, 0) and M (π/a , $\pi/\sqrt{3}a$) for triangular lattice.

In Fig. 1 (a – b), there is one resonator with \bar{N} DOF attached at each unit cell. Each resonator has a stiffness $k_j^{(i)}$ and a mass $m_j^{(i)}$, where $j = 1$ is the index related to the j th resonator and $i = 1, 2, \dots, \bar{N}$ is the index related to the i th DOF in the j th resonator. Fig. 2 illustrates the general case, that is N resonators of \bar{N} DOF attached at the same face of each unit cell, considering

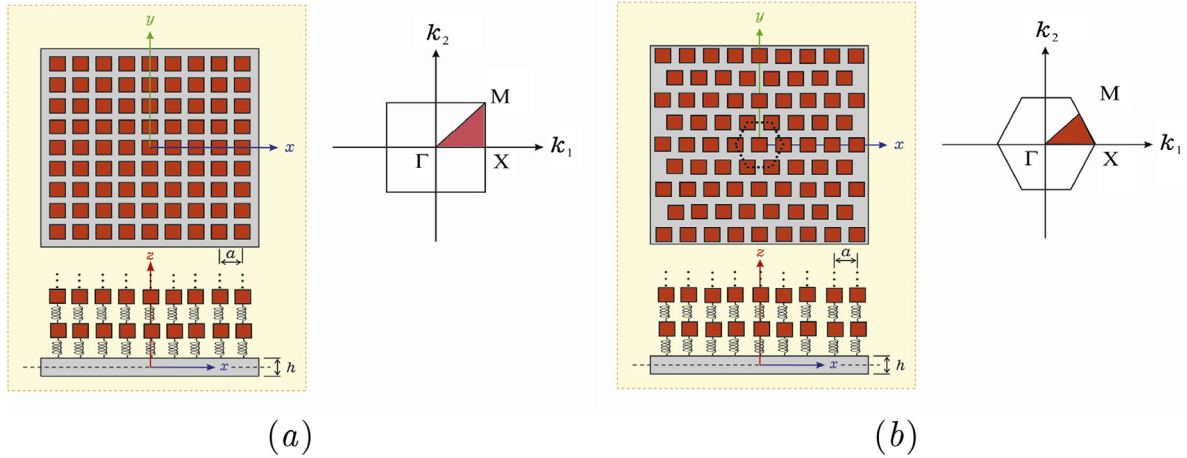


Fig. 1. Infinite elastic metamaterial thin plate with attached single resonator of M-DOF in the unit cell for (a) square and (b) triangular lattices. First irreducible Brillouin zone in shaded region for (a) square and (b) triangular lattices.

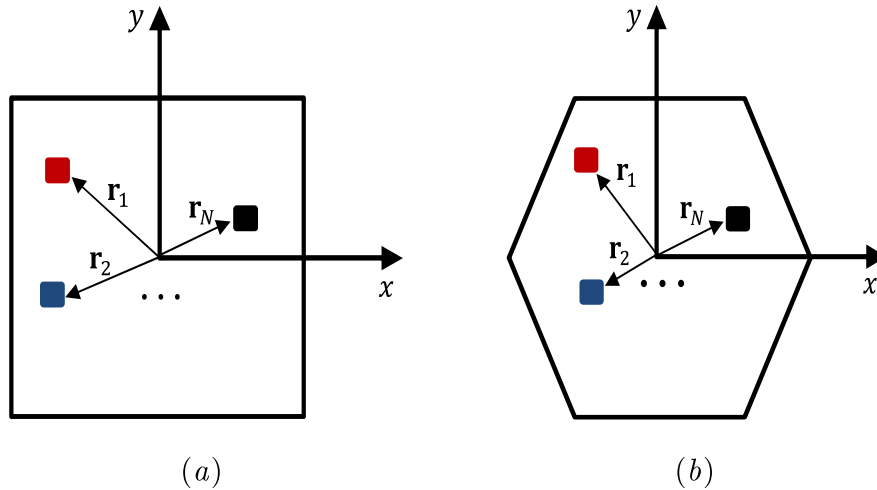


Fig. 2. Unit cell of the elastic metamaterial thin plate with attached multiple resonators of M-DOF for (a) square and (b) triangular lattices.

square (a) and triangular (b) lattices, where $j = 1, 2, \dots, N$ and \mathbf{r}_j is a two-dimensional spatial vector associated with the j th resonator position in the unit cell.

2.1. Plane wave expansion

From Kirchhoff-Love plate theory [62,63], the governing equation for flexural vibration of a uniform thin plate can be written as:

$$D\nabla^2\nabla^2 w(\mathbf{r}, t) + \rho h \frac{\partial^2 w(\mathbf{r}, t)}{\partial t^2} = p(\mathbf{r}, t), \quad (1)$$

where ∇^2 is the Laplacian operator, $D = Eh^3/12(1 - \nu^2)$ is the bending stiffness, E is the Young's modulus, ν is the Poisson's ratio, h is the plate thickness, ρ is the density, $w(\mathbf{r}, t)$ is the transverse displacement, $p(\mathbf{r}, t)$ is the external distributed load, $\mathbf{r} = x\mathbf{e}_1 + y\mathbf{e}_2$ ($x, y \in \mathbb{R}$) is the two-dimensional spatial vector (the system has translational symmetry in z direction, i.e. \mathbf{r} depends only on the x and y coordinates) and \mathbf{e}_i ($i = 1, 2$) are the basis vectors in the real space.

Applying the temporal Fourier transform to Eq. (1) and omitting frequency dependence they produce:

$$D\nabla^2\nabla^2 w(\mathbf{r}) - \omega^2 \rho h w(\mathbf{r}) = p(\mathbf{r}). \quad (2)$$

Now, considering the EM infinite thin plate model (Fig. 1) with attached multiple resonators in the unit cell (Fig. 2), Eq. (2) can be rewritten as,

$$D\nabla^2 \nabla^2 w(\mathbf{r}) - \omega^2 \rho h w(\mathbf{r}) = \sum_{j=1}^N \sum_{\bar{\mathbf{r}}=-\infty}^{+\infty} p_j(\mathbf{r}_j + \bar{\mathbf{r}}) \delta[\mathbf{r} - (\mathbf{r}_j + \bar{\mathbf{r}})], \quad (3)$$

where $\delta[\mathbf{r} - (\mathbf{r}_j + \bar{\mathbf{r}})]$ is the Dirac delta function, $p_j(\mathbf{r}_j + \bar{\mathbf{r}})$ is the force applied to the plate by the j th resonator and $\bar{\mathbf{r}} = \bar{p}\mathbf{a}_1 + \bar{q}\mathbf{a}_2$ ($\bar{p}, \bar{q} \in \mathbb{Z}$) is the lattice vector, \mathbf{a}_i ($i = 1, 2$) are its vectorial components (also known as primitive vectors in real space). The primitive vectors for square lattice are given by $\mathbf{a}_i = a\mathbf{e}_i$ ($i = 1, 2$) and for triangular lattice $\mathbf{a}_1 = a\mathbf{e}_1$, $\mathbf{a}_2 = \frac{a}{2}\mathbf{e}_1 + \frac{a\sqrt{3}}{2}\mathbf{e}_2$.

For attached multiple resonators of S-DOF, the $p_j(\mathbf{r}_j + \bar{\mathbf{r}})$ can be expressed by:

$$p_j(\mathbf{r}_j + \bar{\mathbf{r}}) = k_j^{(1)} [u_j^{(1)}(\mathbf{r}_j + \bar{\mathbf{r}}) - w(\mathbf{r}_j + \bar{\mathbf{r}})], \quad (4)$$

$$-\omega^2 m_j^{(1)} u_j^{(1)}(\mathbf{r}_j + \bar{\mathbf{r}}) = -p_j(\mathbf{r}_j + \bar{\mathbf{r}}), \quad (5)$$

where $u_j^{(i)}(\mathbf{r}_j + \bar{\mathbf{r}})$ and $w(\mathbf{r}_j + \bar{\mathbf{r}})$ are the resonator and plate flexural displacements at position $\mathbf{r}_j + \bar{\mathbf{r}}$, respectively.

Considering attached multiple resonators of \bar{N} DOF in the unit cell (Fig. 2), we have:

$$\omega^2 m_j^{(1)} u_j^{(1)}(\mathbf{r}_j + \bar{\mathbf{r}}) = p_j(\mathbf{r}_j + \bar{\mathbf{r}}) = k_j^{(1)} [u_j^{(1)}(\mathbf{r}_j + \bar{\mathbf{r}}) - w(\mathbf{r}_j + \bar{\mathbf{r}})] - k_j^{(2)} [u_j^{(2)}(\mathbf{r}_j + \bar{\mathbf{r}}) - u_j^{(1)}(\mathbf{r}_j + \bar{\mathbf{r}})], \quad (6a)$$

$$\omega^2 m_j^{(2)} u_j^{(2)}(\mathbf{r}_j + \bar{\mathbf{r}}) = k_j^{(2)} [u_j^{(2)}(\mathbf{r}_j + \bar{\mathbf{r}}) - u_j^{(1)}(\mathbf{r}_j + \bar{\mathbf{r}})] - k_j^{(3)} [u_j^{(3)}(\mathbf{r}_j + \bar{\mathbf{r}}) - u_j^{(2)}(\mathbf{r}_j + \bar{\mathbf{r}})], \quad (6b)$$

⋮

$$\omega^2 m_j^{(\bar{N}-1)} u_j^{(\bar{N}-1)}(\mathbf{r}_j + \bar{\mathbf{r}}) = k_j^{(\bar{N}-1)} [u_j^{(\bar{N}-1)}(\mathbf{r}_j + \bar{\mathbf{r}}) - u_j^{(\bar{N}-2)}(\mathbf{r}_j + \bar{\mathbf{r}})] - k_j^{(\bar{N})} [u_j^{(\bar{N})}(\mathbf{r}_j + \bar{\mathbf{r}}) - u_j^{(\bar{N}-1)}(\mathbf{r}_j + \bar{\mathbf{r}})], \quad (6c)$$

$$\omega^2 m_j^{(\bar{N})} u_j^{(\bar{N})}(\mathbf{r}_j + \bar{\mathbf{r}}) = k_j^{(\bar{N})} [u_j^{(\bar{N})}(\mathbf{r}_j + \bar{\mathbf{r}}) - u_j^{(\bar{N}-1)}(\mathbf{r}_j + \bar{\mathbf{r}})]. \quad (6d)$$

Due to the system periodicity, one can invoke the Floquet-Bloch's theorem [72,73]:

$$w(\mathbf{r}) = e^{i\mathbf{k}\cdot\mathbf{r}} w_{\mathbf{k}}(\mathbf{r}), \quad (7)$$

where $w_{\mathbf{k}}(\mathbf{r})$ is the Bloch wave amplitude. Note that $w_{\mathbf{k}}(\mathbf{r}) = w_{\mathbf{k}}(\mathbf{r} + \bar{\mathbf{r}})$ and $w(\mathbf{r} + \bar{\mathbf{r}}) = w(\mathbf{r})e^{i\mathbf{k}\cdot\bar{\mathbf{r}}}$, where the exponential $e^{i\mathbf{k}\cdot\bar{\mathbf{r}}}$ is called Floquet-Bloch periodic boundary condition and $\mathbf{k} = \bar{u}\mathbf{b}_1 + \bar{v}\mathbf{b}_2$ is the Bloch wave vector, where $(\bar{u}, \bar{v} \in \mathbb{Q})$ are the symmetry points within the FIBZ in reciprocal space or we may write $\mathbf{k} = k_1\mathbf{e}_1 + k_2\mathbf{e}_2$, where $(k_1, k_2 \in \mathbb{R})$ are the point coordinates within the FIBZ for the reciprocal space, considering square and triangular lattices, i.e. Fig. 1 (a–b). The primitive vectors in reciprocal space, i.e. \mathbf{b}_i ($i = 1, 2$), are defined as $\mathbf{b}_1 = 2\pi \frac{\mathbf{a}_2 \times \mathbf{a}_3}{\mathbf{a}_1 \cdot (\mathbf{a}_2 \times \mathbf{a}_3)}$ and $\mathbf{b}_2 = 2\pi \frac{\mathbf{a}_3 \times \mathbf{a}_1}{\mathbf{a}_2 \cdot (\mathbf{a}_3 \times \mathbf{a}_1)}$. In addition, the primitive vectors in real and reciprocal spaces are related by $\mathbf{a}_i \cdot \mathbf{b}_j = 2\pi\delta_{ij}$, $\delta_{ij} = 0$ if $i \neq j$ or $\delta_{ij} = 1$ if $i = j$ is the Kronecker delta.

Expanding $w_{\mathbf{k}}(\mathbf{r})$ in Fourier series on the reciprocal space, one can rewrite Eq. (7) as:

$$w(\mathbf{r}) = e^{i\mathbf{k}\cdot\mathbf{r}} \sum_{\bar{\mathbf{g}}=-\infty}^{+\infty} w(\bar{\mathbf{g}}) e^{i\bar{\mathbf{g}}\cdot\mathbf{r}} = \sum_{\bar{\mathbf{g}}=-\infty}^{+\infty} w(\bar{\mathbf{g}}) e^{i(\mathbf{k}+\bar{\mathbf{g}})\cdot\mathbf{r}}, \quad (8)$$

where $\bar{\mathbf{g}} = \bar{m}\mathbf{b}_1 + \bar{n}\mathbf{b}_2$ is the reciprocal lattice vector and it is calculated for square lattice, i.e. $\bar{\mathbf{g}} = \frac{2\pi}{a}(\bar{m}\mathbf{e}_1 + \bar{n}\mathbf{e}_2)$, and for triangular lattice, i.e. $\bar{\mathbf{g}} = \frac{2\pi}{a}[\bar{m}\mathbf{e}_1 + \frac{(-\bar{m}+2\bar{n})}{\sqrt{3}}\mathbf{e}_2]$, with $(\bar{m}, \bar{n} \in \mathbb{Z})$.

Similarly, applying Floquet-Bloch's theorem [72,73] and expanding in Fourier series on the reciprocal space, the variable $w(\mathbf{r}_j)$ can be written as:

$$w(\mathbf{r}_j) = \sum_{\bar{\mathbf{g}}=-\infty}^{+\infty} w(\bar{\mathbf{g}}) e^{i(\mathbf{k}+\bar{\mathbf{g}})\cdot\mathbf{r}_j}, \quad (9)$$

where $\bar{\mathbf{g}}$ has the same expressions of $\bar{\mathbf{g}}$ for square and triangular lattices, with $(\bar{m}, \bar{n} \in \mathbb{Z})$. From Floquet-Bloch periodic boundary condition, we can write $w(\mathbf{r}_j + \bar{\mathbf{r}})$ and $u_j^{(i)}(\mathbf{r}_j + \bar{\mathbf{r}})$ as:

$$w(\mathbf{r}_j + \bar{\mathbf{r}}) = w(\mathbf{r}_j) e^{i\mathbf{k}\cdot\bar{\mathbf{r}}}, \quad (10)$$

$$u_j^{(i)}(\mathbf{r}_j + \bar{\mathbf{r}}) = u_j^{(i)}(\mathbf{r}_j) e^{i\mathbf{k}\cdot\bar{\mathbf{r}}}. \quad (11)$$

Substituting Eqs. (6a), (8)–(11) in Eq. (3) and after some mathematical manipulations described in Appendix A, one may write:

$$(\mathbf{K} - \omega^2 \mathbf{M})\mathbf{q} = \mathbf{0}, \quad (12)$$

where matrices \mathbf{K} , \mathbf{M} and vector \mathbf{q} are expressed in Appendix A.

Eq. (12) represents a generalized eigenvalue problem of $\omega(\mathbf{k})$. This equation must be solved for each Bloch wave vector into the FIBZ, considering square and triangular lattices. For each value of the Bloch wave vector, $(2M + 1)^2 + \bar{N}N$ eigenvalues are obtained.

2.2. Extended plane wave expansion

The equation of motion of the j th resonator in Fig. 2 can be written as [45]:

$$(\mathbf{K}_j - \omega^2 \mathbf{M}_j) \mathbf{u}_j = \mathbf{p}_j, \quad (13)$$

with the stiffness matrix of the j th resonator given by:

$$\mathbf{K}_j = \begin{bmatrix} k_j^{(1)} & \mathbf{K}_{ji} \\ \mathbf{K}_{ji}^T & \mathbf{K}_{jj} \end{bmatrix}, \quad (14)$$

where the sub-matrices are given by:

$$\mathbf{K}_{ji} = \mathbf{K}_{ji}^T = \begin{bmatrix} -k_j^{(1)} & 0 & 0 & \dots & 0 \end{bmatrix}^T, \quad (15)$$

$$\mathbf{K}_{jj} = \begin{bmatrix} k_j^{(1)} + k_j^{(2)} & -k_j^{(2)} & 0 & 0 & \dots & 0 \\ -k_j^{(2)} & k_j^{(2)} + k_j^{(3)} & -k_j^{(3)} & 0 & \dots & 0 \\ 0 & -k_j^{(3)} & k_j^{(3)} + k_j^{(4)} & -k_j^{(4)} & \ddots & 0 \\ \vdots & \vdots & \ddots & \ddots & \ddots & \vdots \\ 0 & 0 & \dots & -k_j^{(\bar{N}-1)} & k_j^{(\bar{N}-1)} + k_j^{(\bar{N})} & -k_j^{(\bar{N})} \\ 0 & 0 & 0 & \dots & -k_j^{(\bar{N})} & k_j^{(\bar{N})} \end{bmatrix}. \quad (16)$$

Assuming zero mass at the attachment point between the j th resonator and the EM thin plate, the mass matrix can be expressed as:

$$\mathbf{M}_j = \begin{bmatrix} 0 & \mathbf{0} \\ \mathbf{0} & \mathbf{M}_{ji} \end{bmatrix}, \quad (17)$$

where the sub-matrix \mathbf{M}_{ji} is written as:

$$\mathbf{M}_{ji} = \text{diag}(m_j^{(1)}, m_j^{(2)}, \dots, m_j^{(\bar{N})}). \quad (18)$$

The displacement vector of the metamaterial system is given by:

$$\mathbf{u}_j = \begin{Bmatrix} w(\mathbf{r}_j + \bar{\mathbf{r}}) \\ \mathbf{u}_{ji} \end{Bmatrix}, \quad (19)$$

where $w(\mathbf{r}_j + \bar{\mathbf{r}})$ is the plate displacement at the attachment point and the displacement vector of the j th resonator is given by:

$$\mathbf{u}_{ji} = \begin{Bmatrix} u_j^{(1)} & u_j^{(2)} & \dots & u_j^{(\bar{N})} \end{Bmatrix}^T. \quad (20)$$

The force vector of the metamaterial system is given by:

$$\mathbf{p}_j = \begin{Bmatrix} -p_j(\mathbf{r}_j + \bar{\mathbf{r}}) \\ \mathbf{p}_{ji} \end{Bmatrix}, \quad (21)$$

where $-p_j(\mathbf{r}_j + \bar{\mathbf{r}})$ is the plate reaction force at the attachment point and the force vector of the j th resonator is given by:

$$\mathbf{p}_{ji} = \begin{Bmatrix} p_j^{(1)} & p_j^{(2)} & \dots & p_j^{(\bar{N})} \end{Bmatrix}^T. \quad (22)$$

Since there are no external forces acting on the resonator masses (Fig. 2), i.e. $\mathbf{p}_{ji} = \mathbf{0}$ and the metamaterial displacement vector can be condensed. Thus, Eq. (13) can be rewritten as:

$$p_j(\mathbf{r}_j + \bar{\mathbf{r}}) = -D_j w(\mathbf{r}_j + \bar{\mathbf{r}}), \quad (23)$$

where D_j is the dynamic stiffness of the j th resonator given by:

$$D_j = k_j^{(1)} - \mathbf{K}_{ji}(\mathbf{K}_{ji} - \omega^2 \mathbf{M}_{ji})\mathbf{K}_{ji}. \quad (24)$$

To find the natural frequency of the j th resonator, $\omega_j^{(i)}$, the following problem must be solved:

$$|\mathbf{K}_{ji} - \omega^2 \mathbf{M}_{ji}| = 0. \quad (25)$$

In order to include damping in the resonator, a complex stiffness is used, i.e. $k_j^{(i)} = k_j^{(i)}(1 + i\eta_j^{(i)})$, where $\eta_j^{(i)}$ is the damping of the j th resonator, also known as loss factor.

To obtain the EPWE formulation, Eq. (23) is substituted into the Eq. (3), producing:

$$D\nabla^2 \nabla^2 \mathbf{w}(\mathbf{r}) - \omega^2 \rho h \mathbf{w}(\mathbf{r}) + \sum_{j=1}^N \sum_{\mathbf{r}=-\infty}^{+\infty} D_j \mathbf{w}(\mathbf{r}_j + \mathbf{r}) \delta[\mathbf{r} - (\mathbf{r}_j + \mathbf{r})] = 0. \quad (26)$$

Inserting Eqs. (8)–(10) in (26) and after some mathematical manipulations described in Appendix B, one may write a standard eigenvalue problem:

$$\begin{bmatrix} -\mathbf{A}_3 & \mathbf{A}_2 & -\mathbf{A}_1 & -\mathbf{A}_0 \\ \mathbf{I} & \mathbf{0} & \mathbf{0} & \mathbf{0} \\ \mathbf{0} & \mathbf{I} & \mathbf{0} & \mathbf{0} \\ \mathbf{0} & \mathbf{0} & \mathbf{I} & \mathbf{0} \end{bmatrix} \begin{Bmatrix} \bar{k}^3 \mathbf{w}(\mathbf{g}) \\ \bar{k}^2 \mathbf{w}(\mathbf{g}) \\ \bar{k} \mathbf{w}(\mathbf{g}) \\ \mathbf{w}(\mathbf{g}) \end{Bmatrix} = \bar{k} \begin{Bmatrix} \bar{k}^3 \mathbf{w}(\mathbf{g}) \\ \bar{k}^2 \mathbf{w}(\mathbf{g}) \\ \bar{k} \mathbf{w}(\mathbf{g}) \\ \mathbf{w}(\mathbf{g}) \end{Bmatrix}, \quad (27)$$

where vector $\mathbf{w}(\mathbf{g})$ is defined in Eq. (A.22), $\bar{k} = ka$ and matrices $\mathbf{A}_0, \mathbf{A}_1, \mathbf{A}_2$ and \mathbf{A}_3 are given in Appendix B. For a given frequency ω and an azimuth angle ϕ of the Bloch wave vector, there are $4(2M+1)^2$ eigenvalues \bar{k} . Eq. (27) represents a generalized eigenvalue problem of $\mathbf{k}(\omega)$. The main advantage of EPWE method as compared to PWE method is to obtain the complex values of \mathbf{k} , which are related to the evanescent waves and metamaterial system attenuation, since attenuation of the unit cell is defined as $\mu = \Im\{\mathbf{k}\}a$.

Alternative models for an EM thin plate with resonators of M-DOF were considered by Haslinger et al. [56], that is to say multiple mass-spring resonators attached to both faces of the plate and Winkler-type foundation, the masses are embedded within the top surface of the plate. These cases can be interesting for future experimental and EPWE extensions.

3. Simulated examples

To verify the PWE and EPWE methods formulated with Kirchhoff-Love plate theory [62,63] and to demonstrate their capacity of calculating the complex band structure of an infinite EM thin plate with attached multiple resonators of M-DOF, simulated examples are performed in this section. Different configurations related to the number of attached resonators and number of DOF of each resonator are also evaluated.

For all examples, EM thin plate geometry and material properties are the same as shown in Table 1. They are chosen to be the same as used by Xiao and co-workers [49] for the simplest case (EM thin plate with attached single resonator of S-DOF, considering square lattice), in order to facilitate comparison.

In order to include structural damping in the EM thin plate, a complex Young's modulus is used, i.e. $E = E(1 + i\eta)$. Hereafter, the resonators are localized on the middle of unit cell for all simulated examples. Thus, when there are two or more resonators in the unit cell, we considered all of them in the middle of unit cell, i.e. $\mathbf{r}_j = \mathbf{0}$, for mathematical simplification. We also highlight that this does not mean that the resonators are attached above and below the EM plate, at the same spatial point, since in our modelling the resonators are attached on the same face of the EM plate.

It is important to highlight that we apply a criterion for tracking the frequency evolution of wave modes when EPWE method is used. In EPWE method the wave modes are computed at several discrete frequencies. Then, another issue is to associate, among all modes defined at a given frequency $(\omega + \Delta\omega)$, the one which matches a given mode defined at the previous frequency (ω) .

Table 1
Elastic metamaterial thin plate geometry and material properties.

Geometry/Property	Value
Lattice parameter (a)	0.1 m
Unit cell area for square lattice ($S = a^2$)	0.01 m ²
Unit cell area for triangular lattice ($S = a^2\sqrt{3}/2$)	0.0087 m ²
Thickness (h)	0.002 m
Young's modulus (E)	70×10^9 Pa
Mass density (ρ)	2700 kg/m ³
Structural damping (η)	0.01
Poisson's ratio (ν)	0.3

We choose the model assurance criterion (MAC) to estimate the correlation among wave shapes. This criterion is based on the hermitian scalar product and it is useful for very low frequencies [74]. Given a wave shape l defined at a specific frequency ω and for a sufficiently small $\Delta\omega$, the wave shape l defined at frequency $\omega + \Delta\omega$ results:

$$\left| \frac{\Phi_l^H(\omega)}{\|\Phi_l(\omega)\|} \frac{\Phi_l(\omega + \Delta\omega)}{\|\Phi_l(\omega + \Delta\omega)\|} \right| = \max_s \left\{ \left| \frac{\Phi_l^H(\omega)}{\|\Phi_l(\omega)\|} \frac{\Phi_s(\omega + \Delta\omega)}{\|\Phi_s(\omega + \Delta\omega)\|} \right| \right\}, \quad (28)$$

where $\|\Phi_l\| = \sqrt{\Phi_l^H \Phi_l}$ denotes the hermitian norm of the eigenvectors Φ_l , which can be related to Eq. (27) by:

$$\Phi_l = \begin{Bmatrix} \bar{k}^3 \mathbf{w}(\mathbf{g}) \\ \bar{k}^2 \mathbf{w}(\mathbf{g}) \\ \bar{k} \mathbf{w}(\mathbf{g}) \\ \mathbf{w}(\mathbf{g}) \end{Bmatrix}_l, \quad (29)$$

with $l, s = 1, \dots, 4(2M+1)^2$ and $(\cdot)^H$ indicates the conjugate transpose. From now on, band structures calculated by EPWE are ordered using MAC.

For all PWE and EPWE calculations from now on, 81 plane waves, *i.e.* ($M = 4$), are used for Fourier series expansion. This resulted in a good convergence.

3.1. Single resonator of S-DOF – SRSD

In the first example, we consider the simplest case, *i.e.* an EM thin plate with an attached single resonator of S-DOF (SRSD) in the unit cell. S-DOF resonator parameters are: $\eta_1^{(1)} = 0.05$, $f_1^{(1)} = 300$ Hz, $m_1^{(1)} = \gamma_1^{(1)} \rho S a$, where $\gamma_1^{(1)} = 0.5$ is the ratio of resonator mass to the plate unit cell mass. Resonator stiffness is calculated by $k_1^{(1)} = m_1^{(1)} (2\pi f_1^{(1)})^2 (1 + i\eta_1^{(1)})$.

Fig. 3 shows the band structure real part of the EM thin plate for square (a) and triangular (b) lattices calculated by PWE method. The band structure for square lattice agrees with the results of Xiao and co-workers [49]. Moreover, Fig. 3 is clearly reminiscent of both Figs. 4 and A3 in the appendix of Haslinger et al. [56] for the square lattice.

In Fig. 3 we plot the band structure real part in the three principal symmetry directions of the FIBZ. The plots are given in terms of frequency in Hz versus the real part of the reduced Bloch wave vector defined as $\mathbf{k}a/2\pi$. One complete locally resonant band gap is found around the resonant frequency of 300 Hz for both lattices.

Bragg-type band gap is predicted by Bragg's law along different directions, *i.e.* $a = n(\lambda/2 \cos \phi)$ ($n \in \mathbb{Z}$). For a thin plate, the first Bragg frequency, that is to say $n = 1$, is given by:

$$f_{B_1} = \frac{1}{2\pi} \left(\frac{\pi}{a \cos \phi} \right)^2 \sqrt{\frac{D}{\rho h}} = \frac{1}{2\pi} \left\{ \frac{\pi}{a \cos[\arctan(k_2/k_1)]} \right\}^2 \sqrt{\frac{D}{\rho h}}. \quad (30)$$

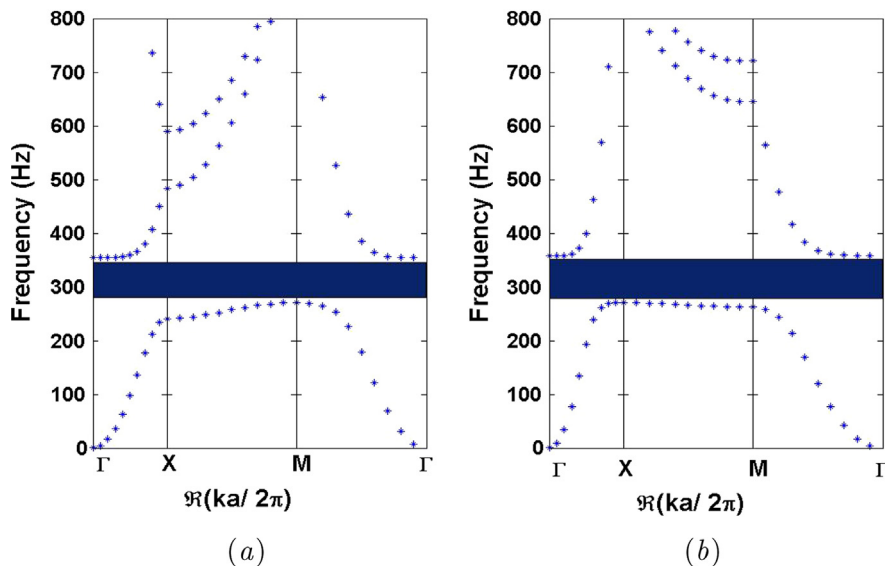


Fig. 3. Elastic band structure real parts of EM thin plate for (a) square and (b) triangular lattices considering $f_1^{(1)} = 300$ Hz and the data of Table 1.

The first Bragg frequency for square lattice along ΓX direction ($\phi = 0^\circ$) calculated by Eq. (30) is 484 Hz and it can be observed in Fig. 3 (a). This Bragg-type band gap creates a directional (partial) band gap along ΓX direction. Along $M\Gamma$ direction ($\phi = 45^\circ$) the first Bragg frequency is 968 Hz. However, along XM direction we have a variation of ϕ , thus f_{B_1} also varies. For triangular lattice, the first Bragg frequency along $M\Gamma$ direction ($\phi = 30^\circ$) is 645.4 Hz and a directional band gap is opened up, as illustrated in Fig. 3 (b).

Fig. 4 compares the elastic band structure real part of square and triangular lattices. We observe that triangular lattice presents a broader complete locally resonant band gap than square lattice. The bandwidth for triangular lattice is 89.4 Hz while the bandwidth for square lattice is 84.3 Hz.

Fig. 5 (a-b) illustrates the elastic band structure imaginary parts for square and triangular lattices, respectively, calculated by EPWE method. In Fig. 5 (a-b), we consider only the smallest positive imaginary part of the reduced Bloch wave vector (lowest component whose real part of the reduced Bloch wave vector lies inside and around the FIBZ is the most accurate), since it represents the least rapidly decaying wave (evanescent Bloch wave [68–70]) that carries energy the farthest [49].

Elastic band structure imaginary part for square lattice in Fig. 5 (a) agrees with the results of Xiao and co-workers [49]. From Fig. 5 (a-b), it can be seen the locally resonant and the Bragg-type band gaps for square and triangular lattices in different directions. Locally resonant band gaps for triangular lattice do not vary with ϕ , differently from square lattice. These results complement the elastic band structure real parts for square and triangular lattices illustrated in Fig. 4 (a-b).

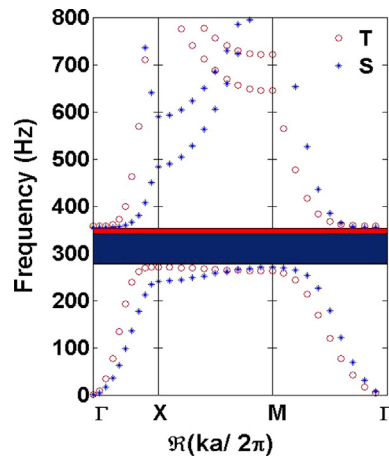


Fig. 4. Comparison of elastic band structure real parts of EM thin plate for square (S) and triangular (T) lattices considering $f_1^{(1)} = 300$ Hz and the data of Table 1.

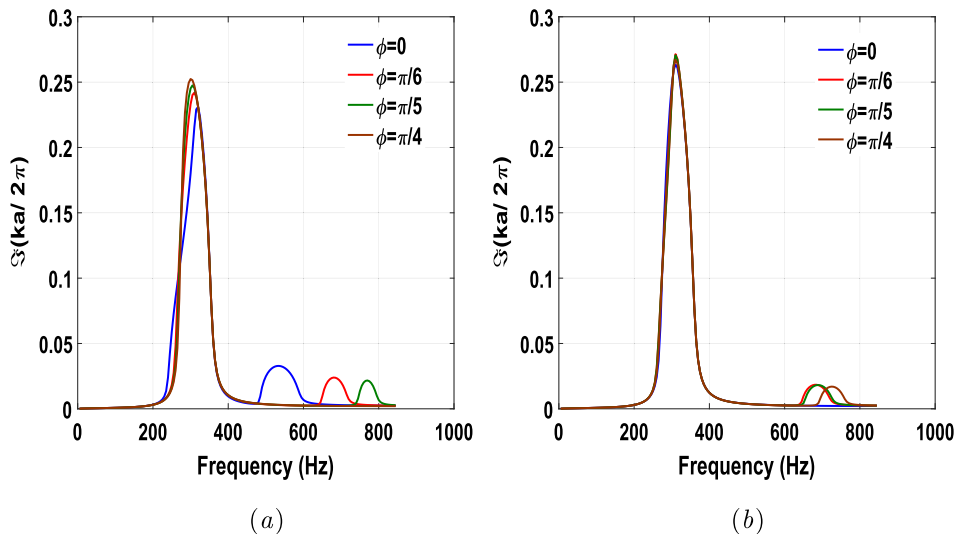


Fig. 5. Elastic band structure imaginary parts of EM thin plate for (a) square and (b) triangular lattices considering $f_1^{(1)} = 300$ Hz and the data of Table 1.

Fig. 6 compares the unit cell attenuation performance of square and triangular lattices. Locally resonant band gap attenuation related to triangular lattice is little higher than square lattice. However, Bragg-type band gap attenuation is higher for square lattice.

3.2. Multiple resonators of S-DOF – MRSD

In this subsection, we consider an EM thin plate with attached multiple resonators of S-DOF (MRSD) in the unit cell. The S-DOF local resonator parameters are $f_j^{(1)} = \{283, 102\}$ Hz, $\gamma_j^{(1)} = 0.5 \times \{0.6, 0.4\}$, $m_j^{(1)} = \gamma_j^{(1)} \rho S a$, $\eta_j^{(1)} = 0.05$ and $k_j^{(1)} = m_j^{(1)} (2\pi f_j^{(1)})^2 (1 + i\eta_j^{(1)})$, where $j = 1, 2$. From now on, the sum of all ratio of resonator mass to the plate unit cell mass is equal to 0.5, the same as SRSD configuration.

Fig. 7 shows the elastic band structure real parts of the EM thin plate with attached double resonators of S-DOF in the unit cell for square (a) and triangular (b) lattices.

It can be seen the locally resonant band gaps on the natural frequencies of the resonators (283 Hz and 102 Hz). The resonator with natural frequency of 283 Hz opened up the broadest complete locally resonant band gap for both lattices. The

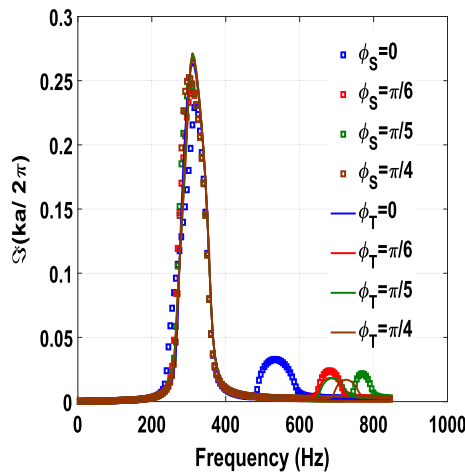


Fig. 6. Comparison of elastic band structure imaginary parts of EM thin plate for square (ϕ_S) and triangular (ϕ_T) lattices considering $f_1^{(1)} = 300$ Hz and the data of Table 1.

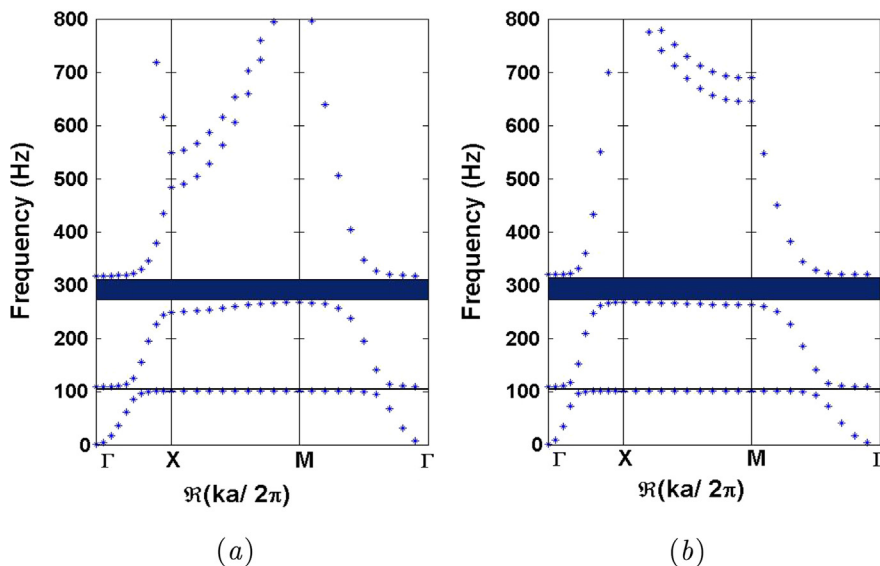


Fig. 7. Elastic band structure real parts of EM thin plate with attached double periodic arrays of S-DOF resonators for (a) square and (b) triangular lattices considering $f_j^{(1)} = \{283, 102\}$ Hz and the data of Table 1.

locally resonant band gap related to the natural frequency 283 Hz is broader for triangular lattice than square lattice, similar as SRSD configuration.

Fig. 8 illustrates the elastic band structure imaginary parts for square (a) and triangular (b) lattices, respectively. It can be seen the unit cell attenuation performance of the two locally resonant and the Bragg-type band gaps for square and triangular lattices in different directions. The highest attenuation is related to the resonator with natural frequency of 283 Hz for both lattices.

Fig. 9 compares the attenuation performance of square (a) and triangular (b) lattices. Square and triangular lattices present almost the same attenuation performance on the locally resonant band gaps and the attenuation related to the Bragg-type band gap is higher for square lattice.

One can note that locally resonant and Bragg-type band gaps for SRSD configuration (Fig. 5) presents higher attenuation and are broader than the band gaps for MRSD configuration (Fig. 8).

3.3. Single resonator of M -DOF – SRMD

We consider an EM thin plate with attached single resonator of 2-DOF in the unit cell. The 2-DOF resonator parameters are $\gamma_1^{(i)} = 0.25$, $m_1^{(i)} = \gamma_1^{(i)} \rho S a$, $k_1^{(1)} = m_1^{(1)} (2\pi \times 160)^2 (1 + i\eta_1^{(1)})$, $k_1^{(2)} = m_1^{(2)} (2\pi \times 180)^2 (1 + i\eta_1^{(2)})$ and $\eta_1^{(i)} = 0.05$, where $i = 1, 2$. The natural frequencies of the resonator are calculated by Eq. 25 and results in:

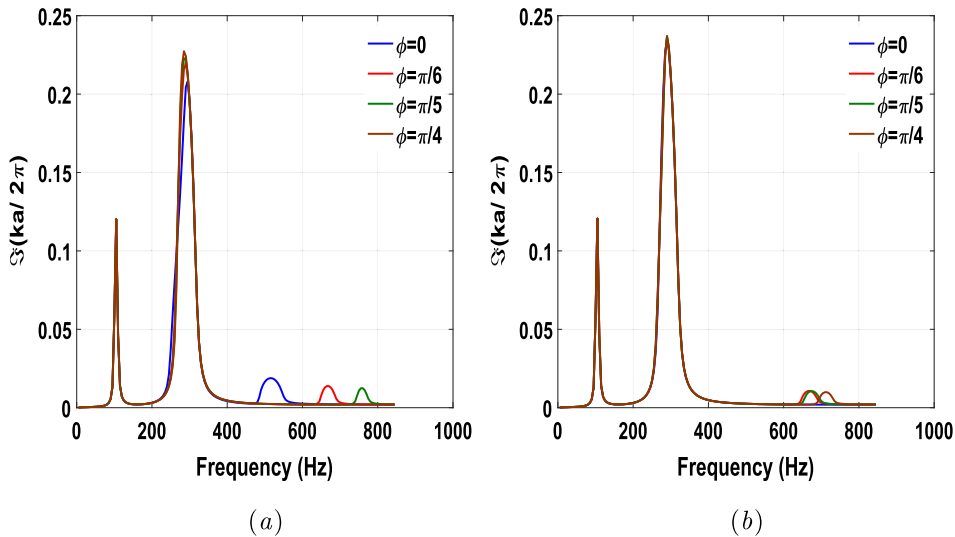


Fig. 8. Elastic band structure imaginary parts of EM thin plate with attached double periodic arrays of S-DOF resonators for (a) square and (b) triangular lattices considering $f_j^{(1)} = \{283, 102\}$ Hz and the data of Table 1.

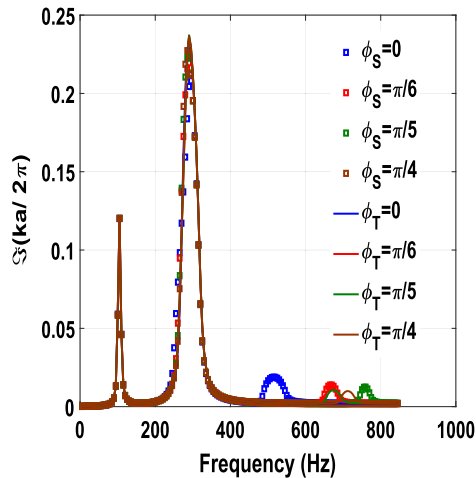


Fig. 9. Comparison of elastic band structure imaginary parts of EM thin plate with attached double periodic arrays of S-DOF resonators for square (ϕ_S) and triangular (ϕ_T) lattices considering $f_j^{(1)} = \{283, 102\}$ Hz and the data of Table 1.

$$\omega_1^{(i)^2} = \frac{(k_1^{(1)} m_1^{(2)} + k_1^{(2)} m_1^{(1)} + k_1^{(2)} m_1^{(2)})}{2m_1^{(1)} m_1^{(2)}} \mp \frac{\sqrt{(k_1^{(1)} m_1^{(2)} + k_1^{(2)} m_1^{(1)} + k_1^{(2)} m_1^{(2)})^2 - 4k_1^{(1)} k_1^{(2)} m_1^{(1)} m_1^{(2)}}}{2m_1^{(1)} m_1^{(2)}}, \quad (31)$$

where $f_1^{(i)} = \omega_1^{(i)}/2\pi$, which gives $f_1^{(i)} = \{102, 283\}$ Hz. We choose the same natural frequencies of MRSD configuration in order to compare.

Fig. 10 shows the elastic band structure real parts of the EM thin plate with attached single resonator of 2-DOF in the unit cell for square (a) and triangular (b) lattices. The locally resonant band gaps present the same width approximately for square and triangular lattices.

Fig. 11 illustrates the elastic band structure imaginary parts for the square (a) and for triangular (b) lattices, respectively. One can see that the higher unit cell attenuation is associated with the first natural frequency, 102 Hz, differently from the behaviour of MRSD configuration illustrated in Fig. 8.

Fig. 12 compares the attenuation performance of square and triangular lattices. Square and triangular lattices present almost the same unit cell attenuation performance on the locally resonant band gaps.

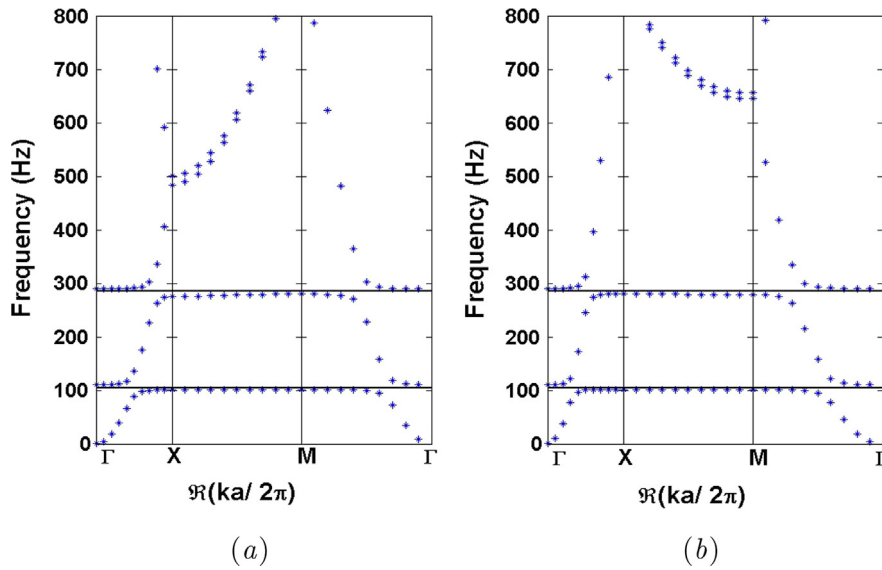


Fig. 10. Elastic band structure real parts of EM thin plate with attached single resonator of 2-DOF in the unit cell for (a) square and (b) triangular lattices considering $f_1^{(i)} = \{102, 283\}$ Hz and the data of Table 1.

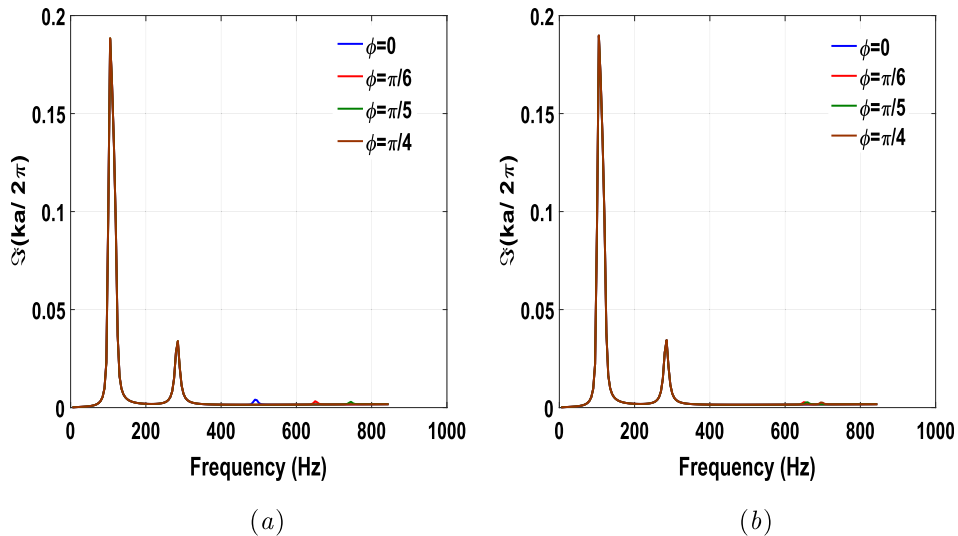


Fig. 11. Elastic band structure imaginary parts of EM thin plate with attached single resonator of 2-DOF in the unit cell for (a) square and (b) triangular lattices considering $f_1^{(i)} = \{102, 283\}$ Hz and the data of Table 1.

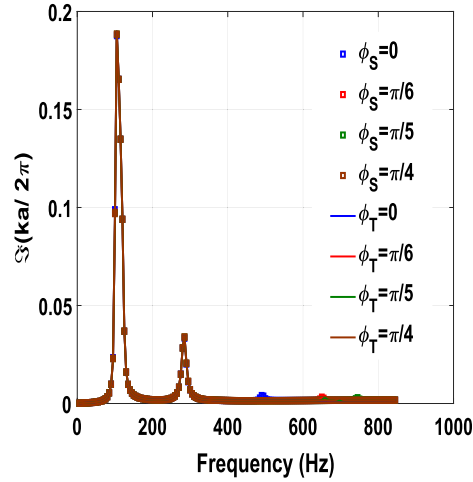


Fig. 12. Comparison of imaginary band structures of EM thin plate with attached single resonator of 2-DOF in the unit cell for square (ϕ_S) and triangular (ϕ_T) lattices considering $f_1^{(i)} = \{102, 283\}$ Hz and the data of Table 1.

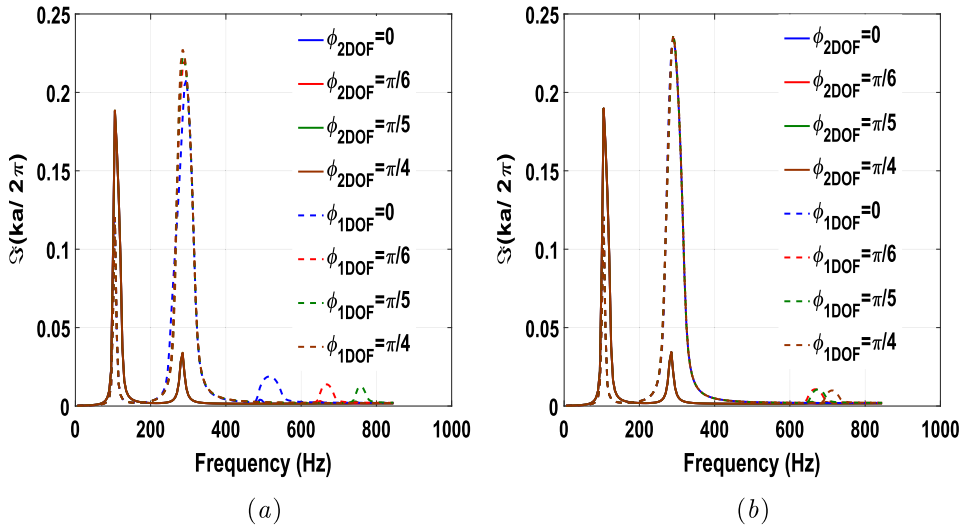


Fig. 13. Comparison of elastic band structure imaginary parts of EM thin plate with attached double resonators of 1-DOF in the unit cell (ϕ_{1DOF}) and with attached single resonator of 2-DOF in the unit cell (ϕ_{2DOF}) for (a) square and (b) triangular lattices, considering $f_j^{(1)} = \{283, 102\}$ Hz and $f_1^{(i)} = \{102, 283\}$ Hz and the data of Table 1.

Fig. 13 shows the elastic band structure imaginary parts of an EM thin plate comparing MRSD and SRMD configurations. Both configurations consider $f_j^{(1)} = \{283, 102\}$ Hz and $f_1^{(i)} = \{102, 283\}$ Hz, respectively, where $i, j = 1, 2$. We can observe that SRMD configuration presents the highest attenuation on 102 Hz for both lattices, whereas MRSD configuration presents higher attenuation than SRMD configuration on 283 Hz. The attenuation related to natural frequency of 283 Hz for MRSD configuration is higher than the attenuation related to natural frequency of 102 Hz for SRMD configuration.

In addition, MRSD configuration provides higher attenuation for Bragg-type band gaps than SRMD configuration, considering square and triangular lattices.

3.4. Multiple resonators of M-DOF – MRMD

In this subsection, we consider an EM thin plate with attached multiple resonators of M-DOF (MRMD) in the unit cell. We regard an EM plate with attached double periodic arrays of 2-DOF resonators. The 2-DOF resonator parameters are $\gamma_j^{(i)} = 0.125$, $m_j^{(i)} = \gamma_j^{(i)} \rho S a$, $k_1^{(1)} = m_1^{(1)} (2\pi \times 160)^2 (1 + i\eta_1^{(1)})$, $k_1^{(2)} = m_1^{(2)} (2\pi \times 180)^2 (1 + i\eta_1^{(2)})$, $k_2^{(1)} = m_2^{(1)} (2\pi \times 100)^2 (1 + i\eta_2^{(1)})$, $k_2^{(2)} = m_2^{(2)} (2\pi \times 300)^2 (1 + i\eta_2^{(2)})$ and $\eta_j^{(i)} = 0.05$. The natural frequencies of the resonators are calculated by Eq. (31), which give $f_1^{(1)} = 102$ Hz, $f_1^{(2)} = 283$ Hz, $f_2^{(1)} = 70$ Hz and $f_2^{(2)} = 430.5$ Hz.

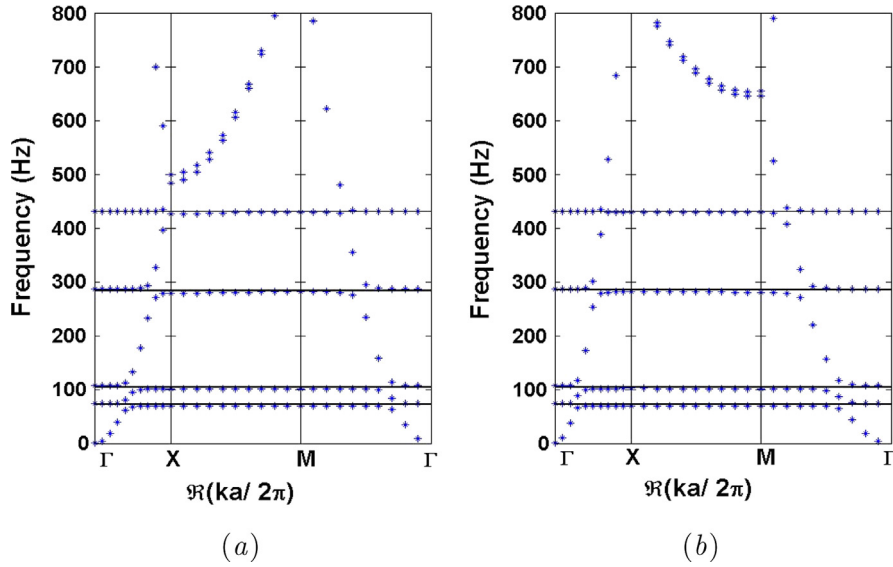


Fig. 14. Elastic band structure real parts of EM thin plate with attached double resonators of 2-DOF in the unit cell for (a) square and (b) triangular lattices, considering $f_1^{(i)} = \{102, 283\}$ Hz and $f_2^{(i)} = \{70, 430.5\}$ Hz and the data of Table 1.

Fig. 14 illustrates the elastic band structure real parts of the EM thin plate with attached double resonators of 2-DOF in the unit cell for square (a) and triangular (b) lattices. We observe four locally resonant band gaps associated with each natural frequency. The narrow locally resonant band gaps present approximately the same width for square and triangular lattices.

Fig. 15 illustrates the elastic band structure imaginary parts for (a) square and (b) triangular lattices, respectively. The highest attenuation is associated with the first natural frequencies, i.e. 70 Hz and 102 Hz. In addition, the locally resonant band gaps on 70 Hz and 102 Hz start to couple. The locally resonant band gap associated with 430.5 Hz has almost no attenuation as well as Bragg-type band gaps.

Fig. 16 compares the unit cell attenuation performance of square and triangular lattices. Square and triangular lattices present almost the same attenuation on the locally resonant band gaps.

Fig. 17 shows the elastic band structure imaginary parts of an EM thin plate comparing MRSD and MRMD configurations. These configurations consider $f_1^{(i)} = \{102, 283\}$ Hz, $f_2^{(i)} = \{70, 430.5\}$ Hz and $f_j^{(1)} = \{70, 102, 283, 430.5\}$ Hz, respectively, where $i = 1, 2$ and $j = 1, 2, 3, 4$.

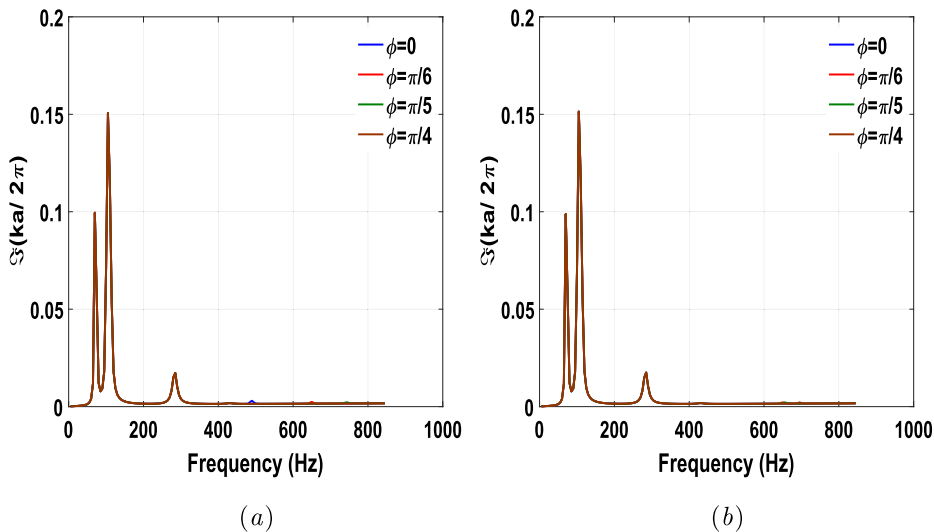


Fig. 15. Elastic band structure imaginary parts of EM thin plate with attached double resonators of 2-DOF in the unit cell for (a) square and (b) triangular lattices considering $f_1^{(i)} = \{102, 283\}$ Hz and $f_2^{(i)} = \{70, 430.5\}$ Hz and the data of Table 1.

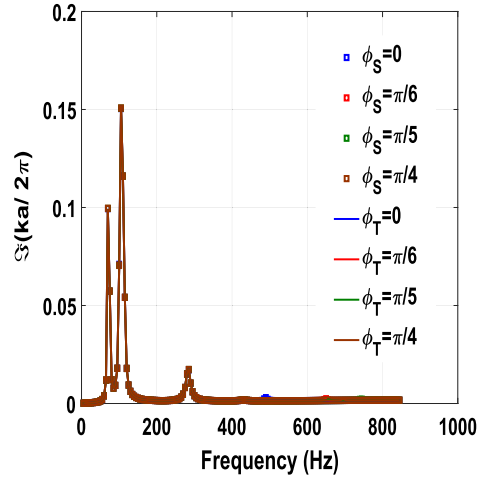


Fig. 16. Comparison of elastic band structure imaginary parts of EM thin plate with attached double resonators of 2-DOF in the unit cell for square (ϕ_S) and triangular (ϕ_T) lattices considering $f_1^{(i)} = \{102, 283\}$ Hz and $f_2^{(i)} = \{70, 430.5\}$ Hz and the data of Table 1.

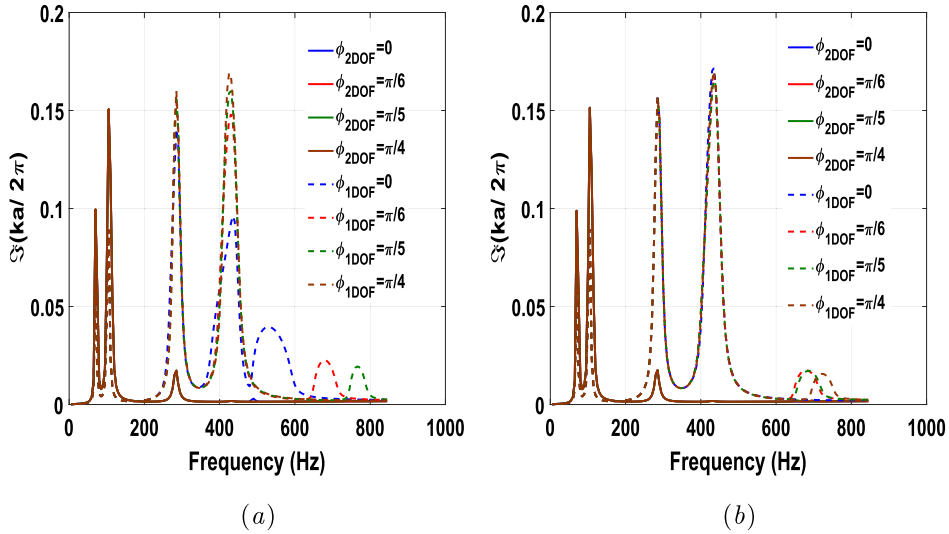


Fig. 17. Comparison of elastic band structure imaginary parts of EM thin plate with attached four resonators of 1-DOF in the unit cell (ϕ_{1DOF}) and with attached double resonators of 2-DOF in the unit cell (ϕ_{2DOF}) for (a) square and (b) triangular lattices, considering $f_j^{(1)} = \{70, 102, 283, 430.5\}$ Hz and $f_1^{(i)} = \{102, 283\}$ Hz, $f_2^{(i)} = \{70, 430.5\}$ Hz.

We can observe that MRMD configuration presents the highest attenuation on 70 Hz and 102 Hz for both lattices. MRSD configuration presents higher attenuation than MRMD configuration on 283 Hz and 430.5. In addition, there is a coupling between the locally resonant and Bragg-type band gaps near 430.5 Hz (see Fig. 17 (a)) for square lattice and $\phi = 0$, considering MRSD configuration. Moreover, MRSD configuration provides higher attenuation for Bragg-type band gaps than MRMD configuration, considering square and triangular lattices.

4. Experimental validation of EM thin plate and numerical verification using FE

In Sections 2 and 3, we consider an infinite EM thin plate by applying Floquet-Bloch periodic boundary condition and calculate the band structures. In this section, frequency response functions (FRFs) are computed for a finite EM plate and a comparison with the band structures of the infinite EM thin plate is provided in order to identify the band gaps. This comparison between infinite and finite metamaterials has been well addressed by many studies [75,76]. However, the comparison between infinite and finite periodic structures is not straightforward in some cases when there is for example the existence of deaf bands [77].

A real EM thin plate with square lattice is used to perform an experimental test. The EM thin plate was designed to be used as a metamaterial plate-like (flexural waves) structures with spatial periodic distribution and local resonators.

Each unit cell of the EM thin plate contains one resonator consisting of a mass ($0.006 \text{ m} \times 0.006 \text{ m} \times 0.0038 \text{ m}$) and a beam ($0.001 \text{ m} \times 0.001 \text{ m} \times 0.002 \text{ m}$) on middle of unit cell that links the mass to the plate. The EM thin plate designed ($0.12 \text{ m} \times 0.096 \text{ m} \times 0.0028 \text{ m}$) was fabricated in a 3D printer and it is illustrated in Fig. 18. One can observe that the EM thin plate contains 10×8 resonators.

The actual EM thin plate geometric parameters and material properties are summarized in Table 2. Material properties, *i.e.* E , ρ and ν , were taken from manufacturer and adjusted in order to numerical results match the experimental results.

For the manufacture of the EM thin plate, an important criterion was observed: the material must be as isotropic as possible. Based on this requirement the EM thin plate was manufactured with plastic material (Vero White Plus) in a 3D printer with UV curing technology.

The measurement instruments used in the experimental setups are summarized in Table 3. The measurements in the EM thin plate were initially performed considering two setups: with a electrodynamic shaker excitation (white noise), Fig. 19

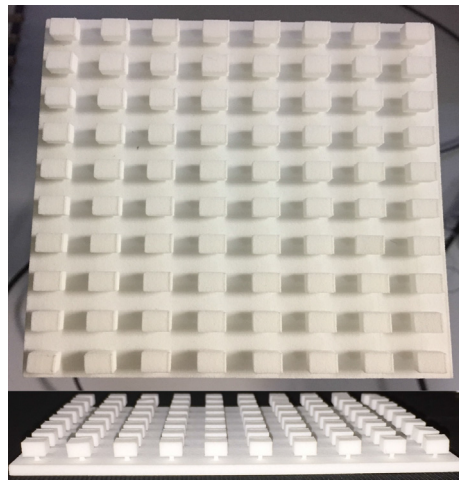


Fig. 18. EM thin plate fabricated in a 3D printer: top and front views.

Table 2
Actual EM thin plate geometry and material properties.

Geometry/Property	Value
Lattice parameter (a)	0.012 m
Total length of the EM thin plate (L_t)	0.12 m
Total length of the resonator mass (L_m)	0.006 m
Total length of the resonator beam (L_b)	0.001 m
Unit cell area ($S = a^2$)	$0.012 \times 0.012 \text{ m}^2$
Cross section area of the EM thin plate ($S = b \times h$)	$0.096 \times 0.0028 \text{ m}^2$
Cross section area of resonator mass ($S_m = b_m \times h_m$)	$0.006 \times 0.0038 \text{ m}^2$
Cross section area of resonator beam ($S_b = b_b \times h_b$)	$0.001 \times 0.002 \text{ m}^2$
Young's modulus (E)	$0.82 \times 10^9 \text{ Pa}$
Mass density (ρ)	600 kg/m^3
Structural damping (η)	0.02
Poisson's ratio (ν)	0.39

Table 3
Measurement instruments.

Instrument	Model	Sensitivity	Measure range
Shaker	TMS K2004E01	–	DC–11 kHz
Force Transducer	PCB 208A02	12.10147 mV/N	0–100 lbs
Hammer	PCB 86E80	23.11 mV/N	222.0 N (peak)
Accelerometer	KISTLER	3.86 mV/g	10 Hz–25 kHz
Data Acquisition	LMS SCR05	–	–

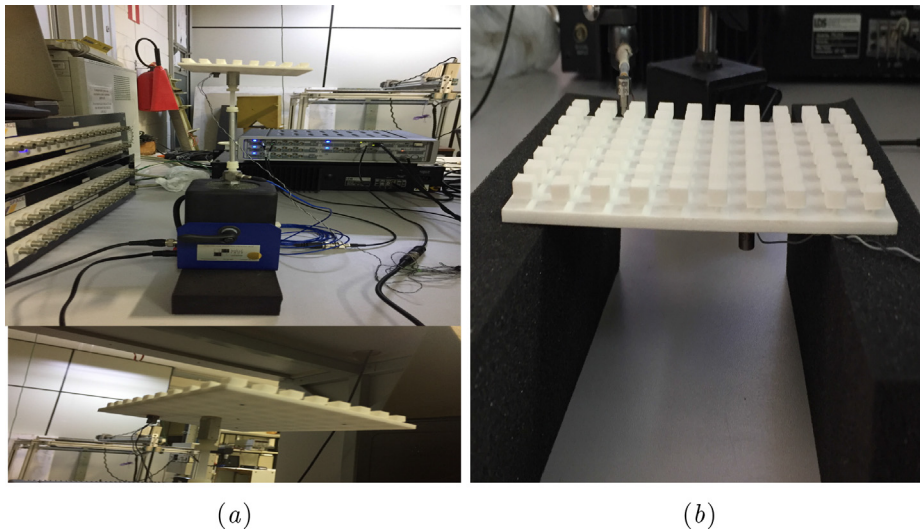


Fig. 19. Experimental setups with the EM thin plate: (a) setup 1 with shaker excitation and (b) setup 2 with hammer excitation.

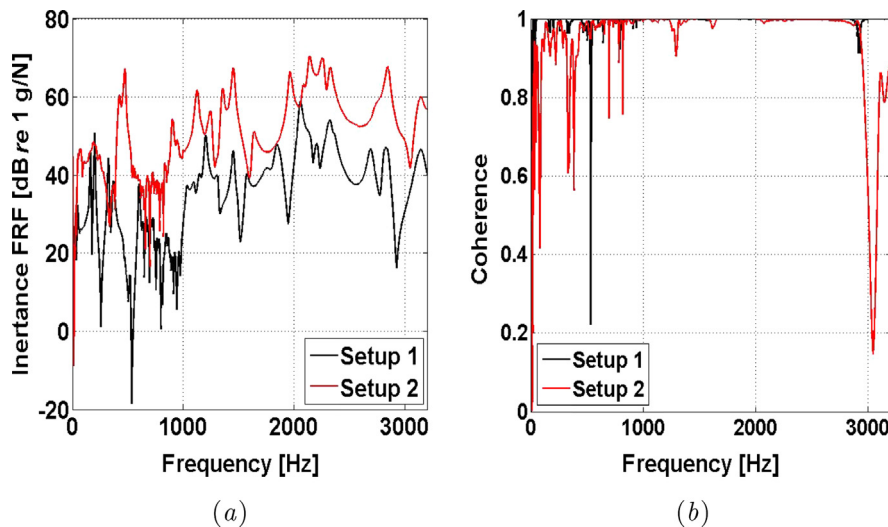


Fig. 20. Typical measured (a) inertance FRFs for setup 1 (black line) and setup 2 (red line) and corresponding (b) ordinary coherence function for setup 1 (black line) and setup 2 (red line). (For interpretation of the references to colour in this figure legend, the reader is referred to the web version of this article.)

(a), and with a impact hammer excitation, Fig. 19 (b), called setups 1 and 2, respectively. The acceleration was obtained by a piezoelectric accelerometer.

Fig. 20 illustrates an example of typical (a) measured transfer inertance FRFs (i.e. acceleration divided by force, also known as accelerance) including the (b) ordinary coherence functions for setups 1 (black line) and 2 (red line). The inertance FRFs for setups 1 and 2 were measured with the LMS SCADAS data acquisition system considering a hundred and five averages, frequency band of 3200 Hz and frequency resolution 0.625 Hz and 0.3906 Hz, respectively. Inertance FRFs for both setups were obtained considering excitation and measurement in different points as illustrated in Fig. 19.

From Fig. 20 (b), it can be observed that setup 1 presents the best coherence. Furthermore, there is a range of frequency in Fig. 20 (a) where a possible locally resonant band gap is opened up. In this range of frequency, there are only flexural evanescent waves. Laude and co-workers [67] defined a complete band gap as a range of frequency whereby all Bloch waves must be evanescent. The evanescent Bloch waves are involved in the diffraction of acoustic phonons at the interfaces of finite PCs [67]. Furthermore, coherence shows bad values in band gap region. We know that this is not a Bragg-type band gap, because

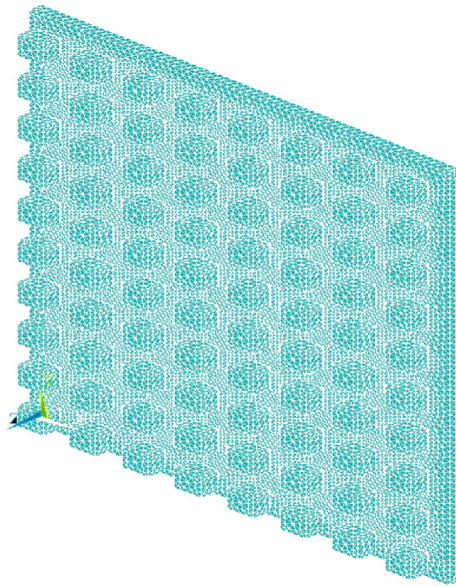


Fig. 21. FE model of the EM thin plate with free edges.

the first Bragg frequency calculated by Eq. (30) for the printed plate without the resonators and $\phi = 0$ is 11194 Hz. From now on, we choose the experimental results of setup 1 in order to compare with the numerical results.

In order to compute the modal analysis and the forced response of the EM thin plate, a commercial finite element analysis software ANSYS (Mechanical APDL Release 14.5) is used. The EM thin plate is modelled with ANSYS using an appropriated element type from its element library, *i.e.* a 3D solid element (SOLID187). The global system is modelled using a free mesh with 158230 triangular elements (3D). The boundary conditions of the actual EM thin plate are free edges. The FE model of EM thin plate is depicted in Fig. 21.

Fig. 22 illustrates the modal analysis of the EM thin plate using FE. We select only the first three flexural modes of the EM thin plate which activate the resonators. Furthermore, only flexural modes of the EM thin plate are excited for the forced response (see the direction of excitation in Fig. 19 a). In Fig. 22, it is illustrated the flexural modes (a) zx in 765.541 Hz, (b) zx in 795.528 Hz and (c) zy in 809.738 Hz. We can also observe in Fig. 22 that resonators absorb most of plate vibration in these frequencies, thus possible locally resonant band gaps are opened up near these frequencies.

The numerical forced response of the EM thin plate is calculated considering the FE modelling described before. We calculated the transmittance among the FRFs in excitation and point (7), *i.e.* inertance point and transfer FRFs, both points are described in Fig. 23.

Fig. 24 compares the transmittance calculated by FE and the real Bloch wave vectors obtained from PWE formulated in Subsection 2.1 from 80 Hz up to 1500 Hz. For PWE calculation, we consider three attached periodic arrays of 1-DOF resonators with $f_j^{(1)} = \{765.541, 795.528, 809.738\}$ Hz from modal analysis in Fig. 22, material properties from Table 2 and 81 plane waves.

PWE identifies three complete locally resonant band gaps in Fig. 24, however, the broadest one is larger than the band gap observed in the transmittance. It can be related to the fact that PWE does not consider the resonator 3D geometry.

We also compute the experimental FRF of the EM thin plate (H_1 estimator) with the LMS SCADAS data acquisition system, considering setup 1 (see Fig. 19 a). We calculated the transmittance among the FRFs in points (2) and (1) described in Fig. 23. Fig. 25 compares the real values of Bloch wave vector calculated by PWE, experimental (Exp) transmittance and transmittance computed by FE.

From PWE results in Fig. 25, it can be observed three complete locally resonant band gaps opened up between 764.9–775.9 Hz, 794.5–808.8 Hz and 803–1080 Hz. Similar as Fig. 24, the broadest locally resonant band gap estimated by PWE is larger than the band gaps in the transmittance obtained by FE and from experimental results, *i.e.* 782–958 Hz and 790–952.5 Hz, respectively.

We remark that FE and experimental transmittance present good agreement, but there is some mismatch. Furthermore, there are uncertainty of the material property values (E and ρ) specified by the plastic manufacturer, which is not guaranteed in the additive manufacturing process used to print the actual EM thin plate.

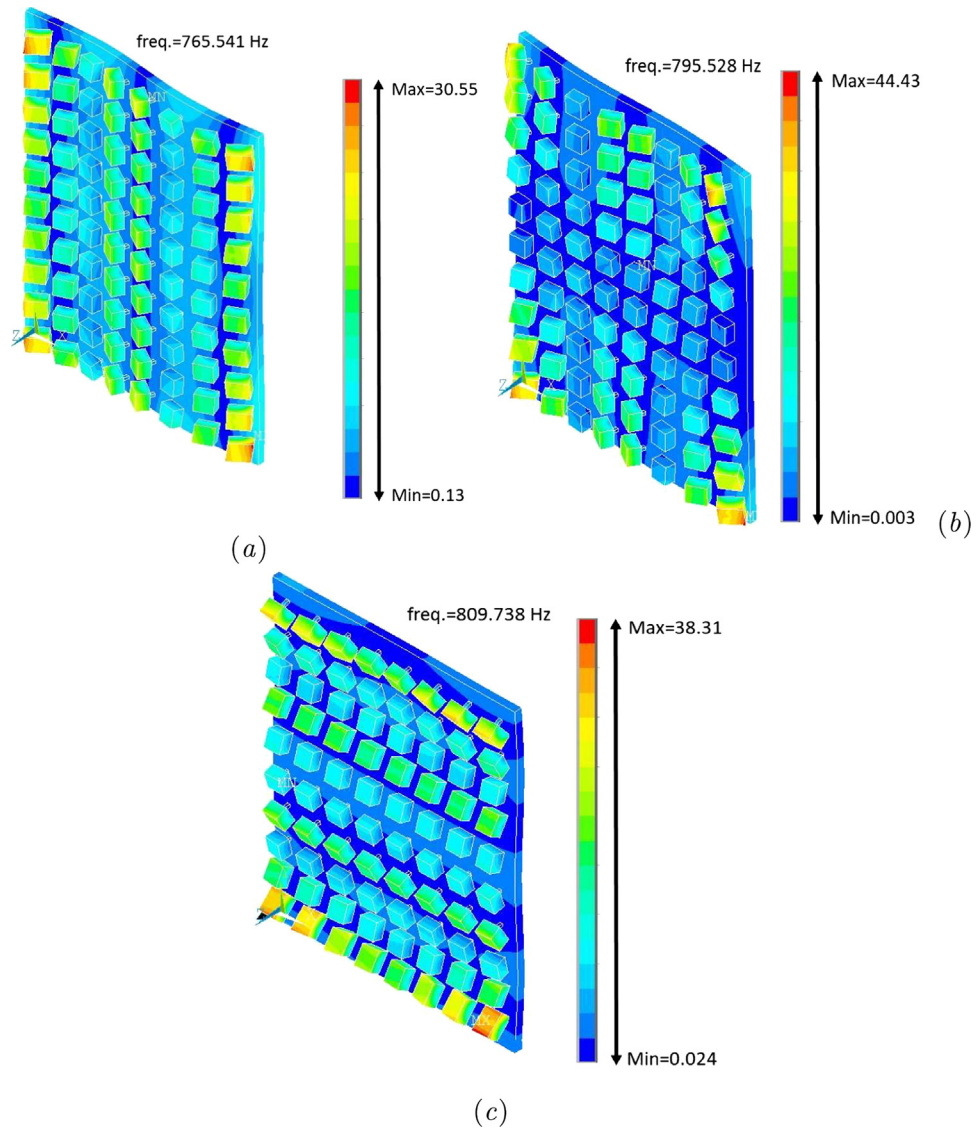


Fig. 22. Modal analysis of the EM thin plate using FE: flexural modes (a) zx in 765.541 Hz, (b) zx in 795.528 Hz and (c) zy in 809.738 Hz.

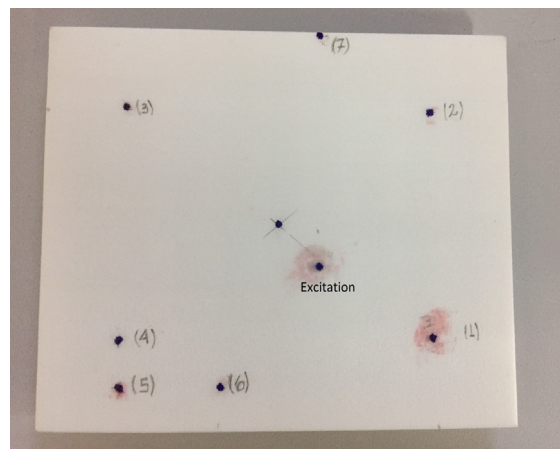


Fig. 23. Localization of excitation with electrodynamic shaker and piezoelectric accelerometer positions denoted by (i).

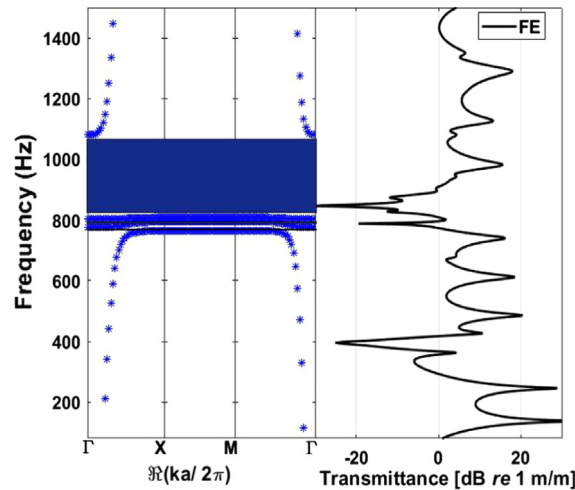


Fig. 24. Comparison of real values of Bloch wave vector calculated by PWE and transmittance computed by FE.

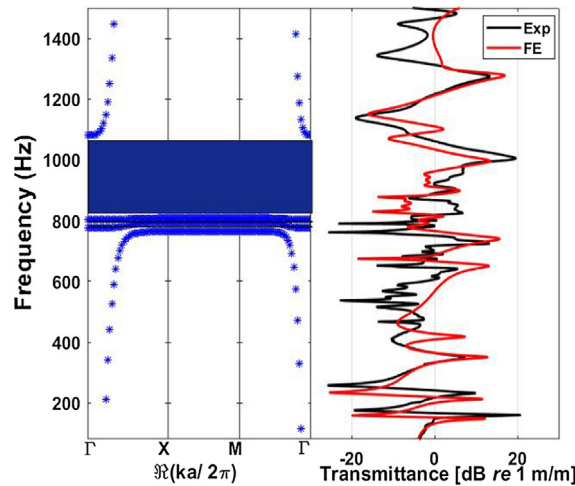


Fig. 25. Comparison of real values of Bloch wave vector calculated by PWE, experimental (Exp) transmittance and transmittance computed by FE.

5. Conclusions

Different configurations of EM thin plates containing multiple resonators of single and multiple degrees of freedom in the unit cell have been investigated in order to open up locally resonant and Bragg-type band gaps. Band gaps are ranges of frequency where there are no mechanical propagating waves, only evanescent waves. These periodic elastic structures started to be proposed in many engineering applications as vibration and noise control devices.

In this study, we proposed semi-analytical formulations using PWE and EPWE methods to deal with an EM thin plate containing multiple resonators of S-DOF and M-DOF in the unit cell, considering square and triangular lattices. Simulated examples have been considered to evaluate four different configurations of EM plates. Complex band structures are calculated by PWE and EPWE using Kirchhoff-Love theory in order to evaluate the EM plate performance in terms of band gap width and unit cell attenuation.

EM thin plates with S-DOF resonators provide higher attenuation for the last locally resonant band gaps (which are opened up for the case of MRSD) and for Bragg-type band gaps than EM thin plates with M-DOF resonators, considering square and triangular lattices. An EM thin plate with square or triangular lattice presents almost the same attenuation performance on the locally resonant band gaps, however, the attenuation related to the Bragg-type band gap is higher for square lattice.

An experimental analysis was conducted with a real EM thin plate with resonators in a square lattice. Modal analysis and forced response are computed by FE method. PWE, FE and experimental results present a good agreement with regard to band gap width.

Acknowledgments

The authors gratefully acknowledge FAPEMA, Project number BM E BD-02591/15, and CAPES for their financial support of this investigation.

Appendix A. Supplement of plane wave expansion formulation

Substituting Eqs. (6a), (8)–(11) in Eq. (3), hereafter, $u_j^{(i)}(\mathbf{r}_j) = u_j^{(i)}$, for brevity, one may write:

$$D \sum_{\mathbf{g}=-\infty}^{+\infty} [(\mathbf{k} + \mathbf{g})_1^2 + (\mathbf{k} + \mathbf{g})_2^2]^2 e^{i(\mathbf{k} + \mathbf{g}) \cdot \mathbf{r}} w(\mathbf{g}) - \omega^2 \rho h \sum_{\mathbf{g}=-\infty}^{+\infty} e^{i(\mathbf{k} + \mathbf{g}) \cdot \mathbf{r}} w(\mathbf{g}) + \sum_{j=1}^N \sum_{\mathbf{r}=-\infty}^{+\infty} k_j^{(1)} e^{i\mathbf{k} \cdot \mathbf{r}} \delta[\mathbf{r} - (\mathbf{r}_j + \mathbf{r})] \sum_{\mathbf{g}=-\infty}^{+\infty} w(\mathbf{g}) e^{i(\mathbf{k} + \mathbf{g}) \cdot \mathbf{r}_j} - \sum_{j=1}^N \sum_{\mathbf{r}=-\infty}^{+\infty} (k_j^{(1)} + k_j^{(2)}) u_j^{(1)} e^{i\mathbf{k} \cdot \mathbf{r}} \delta[\mathbf{r} - (\mathbf{r}_j + \mathbf{r})] + \sum_{j=1}^N \sum_{\mathbf{r}=-\infty}^{+\infty} k_j^{(2)} u_j^{(2)} e^{i\mathbf{k} \cdot \mathbf{r}} \delta[\mathbf{r} - (\mathbf{r}_j + \mathbf{r})] = 0. \quad (\text{A.1})$$

The infinite sum, $\sum_{\mathbf{r}=-\infty}^{+\infty} e^{i\mathbf{k} \cdot \mathbf{r}} \delta[\mathbf{r} - (\mathbf{r}_j + \mathbf{r})]$, in Eq. (A.1) is a periodic function, which can be expanded in Fourier series on the reciprocal space as:

$$\sum_{\mathbf{r}=-\infty}^{+\infty} e^{i\mathbf{k} \cdot \mathbf{r}} \delta[\mathbf{r} - (\mathbf{r}_j + \mathbf{r})] = \sum_{\mathbf{g}=-\infty}^{+\infty} \delta(\mathbf{g}) e^{i\mathbf{g} \cdot \mathbf{r}} = \frac{1}{S} e^{i\mathbf{k} \cdot (\mathbf{r} - \mathbf{r}_j)} \sum_{\mathbf{g}=-\infty}^{+\infty} e^{-i\mathbf{g} \cdot \mathbf{r}_j} e^{i\mathbf{g} \cdot \mathbf{r}}, \quad (\text{A.2})$$

where $\delta(\mathbf{g}) = \frac{1}{S} e^{-i\mathbf{g} \cdot \mathbf{r}_j} e^{i\mathbf{k} \cdot (\mathbf{r} - \mathbf{r}_j)}$ are the Fourier series coefficients and $S = \|\mathbf{a}_1 \times \mathbf{a}_2\|$ is the cross section area of the unit cell. Then, substituting Eq. (A.2) in Eq. (A.1), multiplying by S and rearranging results:

$$DS \sum_{\mathbf{g}=-\infty}^{+\infty} [(\mathbf{k} + \mathbf{g})_1^2 + (\mathbf{k} + \mathbf{g})_2^2]^2 e^{i(\mathbf{k} + \mathbf{g}) \cdot \mathbf{r}} w(\mathbf{g}) + \sum_{j=1}^N \sum_{\mathbf{g}=-\infty}^{+\infty} k_j^{(1)} e^{i(\mathbf{k} + \mathbf{g}) \cdot \mathbf{r}} e^{-i(\mathbf{k} + \mathbf{g}) \cdot \mathbf{r}_j} \sum_{\mathbf{g}=-\infty}^{+\infty} w(\mathbf{g}) e^{i(\mathbf{k} + \mathbf{g}) \cdot \mathbf{r}_j} - \sum_{j=1}^N \sum_{\mathbf{g}=-\infty}^{+\infty} (k_j^{(1)} + k_j^{(2)}) u_j^{(1)} e^{i(\mathbf{k} + \mathbf{g}) \cdot \mathbf{r}} e^{-i(\mathbf{k} + \mathbf{g}) \cdot \mathbf{r}_j} + \sum_{j=1}^N \sum_{\mathbf{g}=-\infty}^{+\infty} k_j^{(2)} u_j^{(2)} e^{i(\mathbf{k} + \mathbf{g}) \cdot \mathbf{r}} e^{-i(\mathbf{k} + \mathbf{g}) \cdot \mathbf{r}_j} - \omega^2 \rho h S \sum_{\mathbf{g}=-\infty}^{+\infty} e^{i(\mathbf{k} + \mathbf{g}) \cdot \mathbf{r}} w(\mathbf{g}) = 0. \quad (\text{A.3})$$

Multiplying Eq. (A.3) by $e^{-i\mathbf{g} \cdot \mathbf{r}}$, where \mathbf{g} has the same expressions of \mathbf{g} for square and triangular lattices, with $(m, n \in \mathbb{Z})$, and integrating over the unit cell results in:

$$DS[(\mathbf{k} + \mathbf{g})_1^2 + (\mathbf{k} + \mathbf{g})_2^2]^2 w(\mathbf{g}) + \sum_{j=1}^N k_j^{(1)} e^{-i(\mathbf{k} + \mathbf{g}) \cdot \mathbf{r}_j} \sum_{\mathbf{g}=-\infty}^{+\infty} w(\mathbf{g}) e^{i(\mathbf{k} + \mathbf{g}) \cdot \mathbf{r}_j} - \sum_{j=1}^N (k_j^{(1)} + k_j^{(2)}) u_j^{(1)} e^{-i(\mathbf{k} + \mathbf{g}) \cdot \mathbf{r}_j} + \sum_{j=1}^N k_j^{(2)} u_j^{(2)} e^{-i(\mathbf{k} + \mathbf{g}) \cdot \mathbf{r}_j} - \omega^2 \rho h S w(\mathbf{g}) = 0. \quad (\text{A.4})$$

Inserting Eqs. (9)–(11) in Eqs. (6a)–(6d), results in:

$$-k_j^{(1)} \sum_{\mathbf{g}=-\infty}^{+\infty} w(\mathbf{g}) e^{i(\mathbf{k} + \mathbf{g}) \cdot \mathbf{r}_j} + (k_j^{(1)} + k_j^{(2)}) u_j^{(1)} - k_j^{(2)} u_j^{(2)} - \omega^2 m_j^{(1)} u_j^{(1)} = 0, \quad (\text{A.5a})$$

$$-k_j^{(2)} u_j^{(1)} + (k_j^{(2)} + k_j^{(3)}) u_j^{(2)} - k_j^{(3)} u_j^{(3)} - \omega^2 m_j^{(2)} u_j^{(2)} = 0, \quad (\text{A.5b})$$

⋮

$$-k_j^{(\bar{N}-1)} u_j^{(\bar{N}-2)} + (k_j^{(\bar{N}-1)} + k_j^{(\bar{N})}) u_j^{(\bar{N}-1)} - k_j^{(\bar{N})} u_j^{(\bar{N})} - \omega^2 m_j^{(\bar{N}-1)} u_j^{(\bar{N}-1)} = 0, \quad (\text{A.5c})$$

$$-k_j^{(\bar{N})} u_j^{(\bar{N}-1)} + k_j^{(\bar{N})} u_j^{(\bar{N})} - \omega^2 m_j^{(\bar{N})} u_j^{(\bar{N})} = 0. \quad (\text{A.5d})$$

Eqs. (A.4) and (A.5a) are an infinite system of equations, thus the Fourier series expansion needs to be truncated. Choosing $m, n, \bar{m}, \bar{n} = [-M, \dots, M]$, the total number of plane waves is $(2M + 1)^2$. Therefore, Eqs. (A.4), (A.5a)–(A.5d) can be expressed in a matrix form as described in Eq. (12).

In Eq. (12), \mathbf{K} is the stiffness matrix of the EM thin plate with multiple periodic arrays of attached M-DOF resonators, which is given by:

$$\mathbf{K} = \begin{bmatrix} \mathbf{K}_{11} & \mathbf{K}_{12} & \mathbf{K}_{13} & \mathbf{0} & \dots & \mathbf{0} \\ \mathbf{K}_{21} & \mathbf{K}_{22} & \mathbf{K}_{23} & \mathbf{0} & \dots & \mathbf{0} \\ \mathbf{0} & \mathbf{K}_{32} & \mathbf{K}_{33} & \mathbf{K}_{34} & \ddots & \mathbf{0} \\ \vdots & \vdots & \ddots & \ddots & \ddots & \vdots \\ \mathbf{0} & \mathbf{0} & \dots & \mathbf{K}_{\bar{N},\bar{N}-1} & \mathbf{K}_{\bar{N},\bar{N}} & \mathbf{K}_{\bar{N},\bar{N}+1} \\ \mathbf{0} & \mathbf{0} & \mathbf{0} & \dots & \mathbf{K}_{\bar{N}+1,\bar{N}} & \mathbf{K}_{\bar{N}+1,\bar{N}+1} \end{bmatrix}. \quad (\text{A.6})$$

The sub-matrices in Eq. (A.6) are expressed by:

$$\mathbf{K}_{11} = D\mathbf{S}\mathbf{Q} + \sum_{j=1}^N k_j^{(1)} \mathbf{U}_j, \quad (\text{A.7})$$

$$\mathbf{K}_{12} = \left[-(k_1^{(1)} + k_1^{(2)})\mathbf{s}_1 \quad \dots \quad -(k_N^{(1)} + k_N^{(2)})\mathbf{s}_N \right], \quad (\text{A.8})$$

$$\mathbf{K}_{13} = \left[k_1^{(1)}\mathbf{s}_1 \quad \dots \quad k_N^{(1)}\mathbf{s}_N \right], \quad (\text{A.9})$$

$$\mathbf{K}_{21} = \left[-k_1^{(1)}\bar{\mathbf{s}}_1 \quad \dots \quad -k_N^{(1)}\bar{\mathbf{s}}_N \right]^T, \quad (\text{A.10})$$

$$\mathbf{K}_{\bar{N}+1,\bar{N}+1} = \text{diag}\left(k_1^{(\bar{N})}, k_2^{(\bar{N})}, \dots, k_N^{(\bar{N})}\right). \quad (\text{A.11})$$

If $i = j$ and $i = 2, 4, \dots, \bar{N}$, sub-matrices are given by:

$$\mathbf{K}_{ii} = \text{diag}\left(k_1^{(i-1)} + k_1^{(i)}, k_2^{(i-1)} + k_2^{(i)}, \dots, k_N^{(i-1)} + k_N^{(i)}\right). \quad (\text{A.12})$$

If $i \neq j$, and $j = i + 1$, sub-matrices are given by:

$$\mathbf{K}_{ij} = \text{diag}\left(-k_1^{(i)}, -k_2^{(i)}, \dots, -k_N^{(i)}\right), \quad i = 2, \dots, \bar{N}, \quad (\text{A.13})$$

and

$$\mathbf{K}_{ji} = \mathbf{K}_{ij}. \quad (\text{A.14})$$

Furthermore, the matrices \mathbf{Q} and \mathbf{U}_j are given by:

$$\mathbf{Q} = \text{diag}\left(\left\{[\mathbf{k} + \bar{\mathbf{g}}_{(-M,-M)}]_1^2 + [\mathbf{k} + \bar{\mathbf{g}}_{(-M,-M)}]_2^2\right\}^2, \left\{[\mathbf{k} + \bar{\mathbf{g}}_{(-M,-M+1)}]_1^2 + [\mathbf{k} + \bar{\mathbf{g}}_{(-M,-M+1)}]_2^2\right\}^2, \dots, \left\{[\mathbf{k} + \bar{\mathbf{g}}_{(M,M)}]_1^2 + [\mathbf{k} + \bar{\mathbf{g}}_{(M,M)}]_2^2\right\}^2\right), \quad (\text{A.15})$$

$$\mathbf{U}_j = \mathbf{s}_j \bar{\mathbf{s}}_j^T, \quad (\text{A.16})$$

where

$$\mathbf{s}_j = \left\{ e^{-i[\mathbf{k} - \bar{\mathbf{g}}_{(-M,-M)}] \cdot \mathbf{r}_j} \quad e^{-i[\mathbf{k} - \bar{\mathbf{g}}_{(-M,-M+1)}] \cdot \mathbf{r}_j} \quad \dots \quad e^{-i[\mathbf{k} - \bar{\mathbf{g}}_{(M,M)}] \cdot \mathbf{r}_j} \right\}^T, \quad (\text{A.17})$$

$$\bar{\mathbf{s}}_j = \left\{ e^{i[\mathbf{k} - \bar{\mathbf{g}}_{(-M,-M)}] \cdot \mathbf{r}_j} \quad e^{i[\mathbf{k} - \bar{\mathbf{g}}_{(-M,-M+1)}] \cdot \mathbf{r}_j} \quad \dots \quad e^{i[\mathbf{k} - \bar{\mathbf{g}}_{(M,M)}] \cdot \mathbf{r}_j} \right\}^T. \quad (\text{A.18})$$

In Eq. (12) \mathbf{M} is the mass matrix of the EM thin plate with attached multiple resonators of M-DOF, which is given by:

$$\mathbf{M} = \begin{bmatrix} \rho h \mathbf{I} & \mathbf{0} & \mathbf{0} & \dots & \mathbf{0} \\ \mathbf{0} & \mathbf{M}_{22} & \mathbf{0} & \dots & \mathbf{0} \\ \mathbf{0} & \mathbf{0} & \mathbf{M}_{33} & \dots & \mathbf{0} \\ \vdots & \vdots & \vdots & \ddots & \vdots \\ \mathbf{0} & \mathbf{0} & \mathbf{0} & \mathbf{0} & \mathbf{M}_{\bar{N}+1,\bar{N}+1} \end{bmatrix}, \quad (\text{A.19})$$

where \mathbf{I} is the identity matrix. If $i = j$ and $i = 2, 4, \dots, \bar{N} + 1$, sub-matrices are given by:

$$\mathbf{M}_{ii} = \text{diag}\left(m_1^{(i-1)}, m_2^{(i-1)}, \dots, m_N^{(i-1)}\right). \quad (\text{A.20})$$

The vector \mathbf{q} in Eq. (12) is the displacement vector of the EM thin plate with attached multiple resonators of M-DOF, which is given by:

$$\mathbf{q} = \left\{ \begin{matrix} \mathbf{w}(\mathbf{g}) \\ \mathbf{u} \end{matrix} \right\}, \quad (\text{A.21})$$

where

$$\mathbf{w}(\mathbf{g}) = \left\{ w[\mathbf{g}_{(-M,-M)}] \quad w[\mathbf{g}_{(-M,-M+1)}] \quad \dots \quad w[\mathbf{g}_{(M,M)}] \right\}^T, \quad (\text{A.22})$$

$$\mathbf{u} = \left\{ u_1^{(1)} \quad \dots \quad u_N^{(1)} \quad u_1^{(2)} \quad \dots \quad u_N^{(2)} \quad u_1^{(\bar{N})} \quad \dots \quad u_N^{(\bar{N})} \right\}^T. \quad (\text{A.23})$$

Appendix B. Supplement of extended plane wave expansion formulation

Inserting Eqs. (8)–(10) in (26), gives:

$$D \sum_{\mathbf{g}=-\infty}^{+\infty} [(\mathbf{k} + \mathbf{g})_1^2 + (\mathbf{k} + \mathbf{g})_2^2] e^{i(\mathbf{k}+\mathbf{g}) \cdot \mathbf{r}} w(\mathbf{g}) - \omega^2 \rho h \sum_{\mathbf{g}=-\infty}^{+\infty} e^{i(\mathbf{k}+\mathbf{g}) \cdot \mathbf{r}} w(\mathbf{g}) + \sum_{j=1}^N \sum_{\mathbf{g}=-\infty}^{+\infty} D_j e^{i(\mathbf{k}+\mathbf{g}) \cdot \mathbf{r}_j} w(\mathbf{g}) \sum_{\mathbf{r}=-\infty}^{+\infty} e^{i\mathbf{k} \cdot \mathbf{r}} \delta[\mathbf{r} - (\mathbf{r}_j + \mathbf{r})]. \quad (\text{B.1})$$

Substituting Eq. (A.2) in Eq. (B.1), multiplying by S and rearranging results:

$$\sum_{\mathbf{g}=-\infty}^{+\infty} \{ DS[(\mathbf{k} + \mathbf{g})_1^2 + (\mathbf{k} + \mathbf{g})_2^2] - \omega^2 \rho h S \} e^{i(\mathbf{k}+\mathbf{g}) \cdot \mathbf{r}} w(\mathbf{g}) + \sum_{j=1}^N \sum_{\mathbf{g}=-\infty}^{+\infty} \sum_{\mathbf{g}=-\infty}^{+\infty} D_j e^{-i(\mathbf{k}+\mathbf{g}) \cdot \mathbf{r}_j} e^{i(\mathbf{k}+\mathbf{g}) \cdot \mathbf{r}_j} e^{i(\mathbf{k}+\mathbf{g}) \cdot \mathbf{r}} w(\mathbf{g}) = 0. \quad (\text{B.2})$$

Multiplying Eq. (B.2) by $e^{-i\mathbf{g} \cdot \mathbf{r}}$ and integrating over the unit cell, it can be rewritten:

$$\{ DS[(\mathbf{k} + \mathbf{g})_1^2 + (\mathbf{k} + \mathbf{g})_2^2] - \omega^2 \rho h S \} w(\mathbf{g}) + \sum_{j=1}^N \sum_{\mathbf{g}=-\infty}^{+\infty} D_j e^{-i(\mathbf{k}+\mathbf{g}) \cdot \mathbf{r}_j} e^{i(\mathbf{k}+\mathbf{g}) \cdot \mathbf{r}_j} w(\mathbf{g}) = 0. \quad (\text{B.3})$$

Similarly as in PWE formulation, Fourier series expansion in Eq. (B.3) are truncated using $m, n, \bar{m}, \bar{n} = [-M, \dots, M]$, and Eq. (B.3) can be rewritten in a matrix form as:

$$(DS\mathbf{Q} - \omega^2 \rho h S \mathbf{I} + \sum_{j=1}^N D_j \mathbf{U}_j) w(\mathbf{g}) = \mathbf{0}. \quad (\text{B.4})$$

We assume that the azimuth angle of the Bloch wave vector is ϕ , thus $\mathbf{k} = k_1 \mathbf{e}_1 + k_2 \mathbf{e}_2 = k \cos \phi \mathbf{e}_1 + k \sin \phi \mathbf{e}_2$, where $k = \|\mathbf{k}\|$ and the elements of matrix \mathbf{Q} in Eq. B.4 can be expanded to obtain:

$$\mathbf{Q} = \frac{1}{a^4} \left[(ka)^4 \mathbf{I} + (ka)^3 \mathbf{X}_3 + (ka)^2 \mathbf{X}_2 + (ka) \mathbf{X}_1 + \mathbf{X}_0 \right], \quad (\text{B.5})$$

where

$$\mathbf{X}_r = \text{diag}(\chi_r(-M, -M), \chi_r(-M, -M+1), \dots, \chi_r(M, M)), \quad (\text{B.6})$$

for $r = 0, 1, 2, 3$ and

$$\chi_0(m, n) = \epsilon_0^2(m, n), \chi_1(m, n) = 2\epsilon_0(m, n)\epsilon_1(m, n), \quad (\text{B.7})$$

$$\chi_2(m, n) = 2\epsilon_0(m, n) + \epsilon_1^2(m, n), \chi_3(m, n) = 2\epsilon_1(m, n), \quad (\text{B.8})$$

$$\epsilon_0(m, n) = [(mb_{11} + nb_{21})a]^2 + [(mb_{12} + nb_{22})a]^2, \quad (\text{B.9})$$

$$\epsilon_1(m, n) = 2[(mb_{11} + nb_{21})a \cos \phi + (mb_{12} + nb_{22})a \sin \phi], \quad (\text{B.10})$$

where $b_{i,2} = \|\mathbf{b}_{i,2}\|$ ($i = 1, 2$). The basis vectors in reciprocal space are $\mathbf{b}_i = \frac{2\pi}{a} \mathbf{e}_i$ ($i = 1, 2$) for square lattice and $\mathbf{b}_1 = \frac{2\pi}{\sqrt{3}a} (\sqrt{3}\mathbf{e}_1 - \mathbf{e}_2)$, $\mathbf{b}_2 = \frac{4\pi}{\sqrt{3}a} \mathbf{e}_2$ for triangular lattice.

Inserting Eq. (B.5) in Eq. (B.4) gives:

$$\left\{ \frac{DS}{a^4} \left[(ka)^4 \mathbf{I} + (ka)^3 \mathbf{X}_3 + (ka)^2 \mathbf{X}_2 + (ka) \mathbf{X}_1 + \mathbf{X}_0 \right] - \omega^2 \rho h S \mathbf{I} + \sum_{j=1}^N D_j \mathbf{U}_j \right\} w(\mathbf{g}) = \mathbf{0}. \quad (\text{B.11})$$

Multiplying Eq. (B.11) by $\frac{a^4}{DS}$ and making $\bar{k} = ka$, $\mathbf{A}_i = \mathbf{X}_i$ ($i = 1, 2, 3$), and

$$\mathbf{A}_0 = \mathbf{X}_0 - \frac{\rho h \omega^2 a^4}{D} \mathbf{I} + \frac{a^4}{DS} \sum_{j=1}^N D_j \mathbf{U}_j, \quad (\text{B.12})$$

it can be rewritten in a compact form as:

$$(\bar{k}^4 \mathbf{I} + \bar{k}^3 \mathbf{A}_3 + \bar{k}^2 \mathbf{A}_2 + \bar{k} \mathbf{A}_1 + \mathbf{A}_0) \mathbf{w}(\mathbf{g}) = \mathbf{0}. \quad (\text{B.13})$$

Eq. (B.13) can be rewritten as a standard eigenvalue problem as shown in Eq. (27).

References

- [1] M.M. Sigalas, E.N. Economou, Elastic and acoustic wave band structure, *J. Sound Vib.* 158 (2) (1992) 377–382, [https://doi.org/10.1016/0022-460X\(92\)90059-7](https://doi.org/10.1016/0022-460X(92)90059-7).
- [2] M.S. Kushwaha, P. Halevi, G. Martinez, L. Dobrzynski, B. Djafari-Rouhani, Theory of acoustic band structure of periodic elastic composites, *Phys. Rev. B* 49 (4) (1994) 2313–2322, <https://doi.org/10.1103/PhysRevB.49.2313>.
- [3] Y. Pennec, J.O. Vasseur, B. Djafari-Rouhani, L. Dobrzynski, P.A. Deymier, Two-dimensional phononic crystals: examples and applications, *Surf. Sci. Rep.* 65 (8) (2010) 229–291, <https://doi.org/10.1016/j.surfrep.2010.08.002>.
- [4] J. Huang, Z. Shi, Attenuation zones of periodic pile barriers and its application in vibration reduction for plane waves, *J. Sound Vib.* 332 (19) (2013) 4423–4439, <https://doi.org/10.1016/j.jsv.2013.03.028>.
- [5] K. Yu, T. Chen, X. Wang, Band gaps in the low-frequency range based on the two-dimensional phononic crystals plates composed of rubber matrix with periodic steel stubs, *Physica B* 416 (2013) 12–16, <https://doi.org/10.1016/j.physb.2013.02.011>.
- [6] N. Gao, J.H. Wu, L. Yu, Research on bandgaps in two-dimensional phononic crystal with two resonators, *Ultrasonics* 56 (2015) 287–293, <https://doi.org/10.1016/j.ultras.2014.08.006>.
- [7] V. Anjos, A. Arantes, Phononic band structure in carbon microtube composites, *RSC Adv.* 5 (15) (2015) 11248–11253, <https://doi.org/10.1039/C4RA12360C>.
- [8] E.J.P. Miranda Jr., J.M.C. Dos Santos, Complete band gaps in nano-piezoelectric phononic crystals, *Mater. Res.* 20 (Suppl. 1) (2017) 15–38, <https://doi.org/10.1590/1980-5373-MR-2017-0298>.
- [9] E.J.P. Miranda Jr., J.M.C. Dos Santos, Band structure in carbon nanostructure phononic crystals, *Mater. Res.* 20 (Suppl. 2) (2017) 555–571, <https://doi.org/10.1590/1980-5373-MR-2016-0898>.
- [10] E.J.P. Miranda Jr., J.M.C. Dos Santos, Flexural wave band gaps in phononic crystal Euler-Bernoulli beams using wave finite element and plane wave expansion methods, *Mater. Res.* 20 (Suppl. 2) (2017) 729–742, <https://doi.org/10.1590/1980-5373-MR-2016-0877>.
- [11] Y. Chen, X. Huang, G. Sun, X. Yan, G. Li, Maximizing spatial decay of evanescent waves in phononic crystals by topology optimization, *Comput. Struct.* 182 (2017) 430–447, <https://doi.org/10.1016/j.compstruc.2017.01.001>.
- [12] L. Xie, B. Xia, J. Liu, G. Huang, J. Lei, An improved fast plane wave expansion method for topology optimization of phononic crystals, *Int. J. Mech. Sci.* 120 (2017) 171–181, <https://doi.org/10.1016/j.ijmecsci.2016.11.023>.
- [13] D. Qian, Z. Shi, Using PWE/FE method to calculate the band structures of the semi-infinite beam-like PCs: periodic in z-direction and finite in x-y plane, *Phys. Lett. A* 381 (2017) 1516–1524, <https://doi.org/10.1016/j.physleta.2017.02.049>.
- [14] M. Mazzotti, M. Miniaci, I. Bartoli, Band structure analysis of leaky Bloch waves in 2D phononic crystal plates, *Ultrasonics* 74 (2017) 140–143, <https://doi.org/10.1016/j.ultras.2016.10.006>.
- [15] O.R. Bilal, A. Foehr, C. Daraio, Observation of trampoline phenomena in 3D-printed metamaterial plates, *Extreme Mech. Lett.* 15 (2017) 103–107, <https://doi.org/10.1016/j.eml.2017.06.004>.
- [16] S. Hedayatrasa, M. Kersemans, K. Abhary, M. Uddin, W.V. Paepegem, Optimization and experimental validation of stiff porous phononic plates for widest complete bandgap of mixed fundamental guided wave modes, *Mech. Syst. Signal Process.* 98 (2018) 786–801, <https://doi.org/10.1016/j.ymssp.2017.05.019>.
- [17] D.-L. Yu, C.-Y. Du, H.-J. Shen, J.-W. Liu, J.-H. Wen, An analysis of structural-acoustic coupling band gaps in a fluid-filled periodic pipe, *Chin. Phys. Lett.* 34 (7) (2017) 076202–076206, <https://doi.org/10.1088/0256-307X/34/7/076202>.
- [18] E.J.P. Miranda Jr., J.M.C. Dos Santos, Evanescent Bloch waves and complex band structure in magnetoelastic phononic crystals, *Mech. Syst. Signal Process.* 112 (2018) 280–304, <https://doi.org/10.1016/j.ymssp.2018.04.034>.
- [19] R.H. Olsson III, I. El-Kady, Microfabricated phononic crystal devices and applications, *Meas. Sci. Technol.* 20 (012002) (2009) 1–13, <https://doi.org/10.1088/0957-0233/20/1/012002>.
- [20] Z. Liu, X. Zhang, Y. Mao, Y.Y. Zhu, Z. Yang, C.T. Chan, P. Sheng, Locally resonant sonic materials, *Science* 289 (5485) (2000) 1734–1736, <https://doi.org/10.1126/science.289.5485.1734>.
- [21] K.M. Ho, C.K. Cheng, Z. Yang, X.X. Zhang, P. Sheng, Broadband locally resonant sonic shields, *Appl. Phys. Lett.* 83 (26) (2003) 5566–5568, <https://doi.org/10.1063/1.1637152>.
- [22] Z. Yang, H.M. Dai, N.H. Chan, G.C. Ma, Acoustic metamaterial panels for sound attenuation in the 50–1000 Hz regime, *Appl. Phys. Lett.* 96 (041906) (2010) 1–3, <https://doi.org/10.1063/1.3299007>.
- [23] F. Casadei, B.S. Beck, K.A. Cunefare, M. Ruzzene, Vibration control of plates through hybrid configurations of periodic piezoelectric shunts, *J. Intell. Mater. Syst. Struct.* 23 (10) (2012) 1169–1177, <https://doi.org/10.1177/1045389X12443014>.
- [24] N. Gao, J.H. Wu, L. Yu, Low frequency band gaps below 10 Hz in radial flexible elastic metamaterial plate, *J. Phys. D: Appl. Phys.* 49 (435501) (2016) 1–9, <https://doi.org/10.1088/0022-3727/49/43/435501>.
- [25] N. Gao, J.H. Wu, L. Yu, H. Xin, Design of radial phononic crystal using annular soft material with low-frequency resonant elastic structures, *Phys. Lett. A* 380 (2016) 3326–3332, <https://doi.org/10.1016/j.physleta.2016.08.010>.
- [26] A.O. Krushynska, M. Miniaci, F. Bosia, N.M. Pugno, Coupling local resonance with Bragg band gaps in single-phase mechanical metamaterials, *Extreme Mech. Lett.* 12 (2017) 30–36, <https://doi.org/10.1016/j.eml.2016.10.004>.
- [27] Y. Li, L. Zhu, T. Chen, Plate-type elastic metamaterials for low-frequency broadband elastic wave attenuation, *Ultrasonics* 73 (2017) 34–42, <https://doi.org/10.1016/j.ultras.2016.08.019>.
- [28] F. Casadei, L. Dozio, M. Ruzzene, K.A. Cunefare, Periodic shunted arrays for the control of noise radiation in an enclosure, *J. Sound Vib.* 329 (18) (2010) 3632–3646, <https://doi.org/10.1016/j.jsv.2010.04.003>.
- [29] Y. Xiao, J. Wen, X. Wen, Sound transmission loss of metamaterial-based thin plates with multiple subwavelength arrays of attached resonators, *J. Sound Vib.* 331 (25) (2012) 5408–5423, <https://doi.org/10.1016/j.jsv.2012.07.016>.
- [30] G. Wang, X. Wen, J. Wen, Y. Liu, Quasi-one-dimensional periodic structure with locally resonant band gap, *J. Appl. Mech.* 73 (1) (2005) 167–170, <https://doi.org/10.1115/1.2061947>.
- [31] Y. Xiao, J. Wen, X. Wen, Longitudinal wave band gaps in metamaterial-based elastic rods containing multi-degree-of-freedom resonators, *New J. Phys.* 14 (033042) (2012) 1–20, <https://doi.org/10.1088/1367-2630/14/3/033042>.
- [32] E.D. Nobrega, F. Gautier, A. Pelat, J.M.C. Dos Santos, Vibration band gaps for elastic metamaterial rods using wave finite element method, *Mech. Syst. Signal Process.* 79 (2016) 192–202, <https://doi.org/10.1016/j.ymssp.2016.02.059>.
- [33] G. Wang, J. Wen, X. Wen, Quasi-one-dimensional phononic crystals studied using the improved lumped-mass method: application to locally resonant beams with flexural wave band gap, *Phys. Rev. B* 71 (104302) (2005) 1–5, <https://doi.org/10.1103/PhysRevB.71.104302>.

- [34] D. Yu, Y. Liu, G. Wang, H. Zhao, J. Qiu, Flexural vibration band gaps in Timoshenko beams with locally resonant structures, *J. Appl. Phys.* 100 (124901) (2006) 1–5, <https://doi.org/10.1063/1.2400803>.
- [35] D. Yu, Y. Liu, H. Zhao, G. Wang, J. Qiu, Flexural vibration band gaps in Euler-Bernoulli beams with locally resonant structures with two degrees of freedom, *Phys. Rev. B* 73 (064301) (2006) 1–5, <https://doi.org/10.1103/PhysRevB.73.064301>.
- [36] Y. Liu, D. Yu, L. Li, H. Zhao, J. Wen, X. Wen, Design guidelines for flexural wave attenuation of slender beams with local resonators, *Phys. Lett. A* 362 (5–6) (2007) 344–347, <https://doi.org/10.1016/j.physleta.2006.10.056>.
- [37] Y. Xiao, J. Wen, X. Wen, Broadband locally resonant beams containing multiple periodic arrays of attached resonators, *Phys. Lett. A* 376 (16) (2012) 1384–1390, <https://doi.org/10.1016/j.physleta.2012.02.059>.
- [38] L. Raghavan, A.S. Phani, Local resonance bandgaps in periodic media: theory and experiment, *J. Acoust. Soc. Am.* 134 (3) (2013) 1950–1959, <https://doi.org/10.1121/1.4817894>.
- [39] M.Y. Wang, X. Wang, Frequency band structure of locally resonant periodic flexural beams suspended with force-moment resonators, *J. Phys. D: Appl. Phys.* 46 (255502) (2013) 1–8, <https://doi.org/10.1088/0022-3727/46/25/255502>.
- [40] Z. Wang, P. Zhang, Y. Zhang, Locally resonant band gaps in flexural vibrations of a Timoshenko beam with periodically attached multioscillators, *Math. Prob. Eng.* 2013 (146975) (2013) 1–10, <https://doi.org/10.1155/2013/146975>.
- [41] Y. Xiao, J. Wen, D. Yu, X. Wen, Flexural wave propagation in beams with periodically attached vibration absorbers: band-gap behavior and band formation mechanisms, *J. Sound Vib.* 332 (4) (2013) 867–893, <https://doi.org/10.1016/j.jsv.2012.09.035>.
- [42] F. Casadei, K. Bertoldi, Wave propagation in beams with periodic arrays of airfoil-shaped resonating units, *J. Sound Vib.* 333 (24) (2014) 6532–6547, <https://doi.org/10.1016/j.jsv.2014.07.008>.
- [43] M.Y. Wang, Y.T. Choy, C.W. Wan, A.S. Zhao, Wide band-gaps in flexural periodic beams with separated force and moment resonators, *J. Vib. Acoust.* 137 (6) (2015) 1–6, <https://doi.org/10.1115/1.4031519>.
- [44] T. Wang, M.P. Sheng, Q.H. Qin, Multi-flexural band gaps in an Euler-Bernoulli beam with lateral local resonators, *Phys. Lett. A* 380 (4) (2016) 525–529, <https://doi.org/10.1016/j.physleta.2015.12.010>.
- [45] E.J.P. Miranda Jr., J.M.C. Dos Santos, Flexural wave band gaps in an elastic metamaterial beam with periodically attached spring-mass resonators, in: *Proceedings of ISMA2016, Leuven, Belgium, 2016*, pp. 2099–2113.
- [46] C. Sugino, Y. Xia, S. Leadenham, M. Ruzzene, A. Erturk, A general theory for bandgap estimation in locally resonant metastructures, *J. Sound Vib.* 406 (2017) 104–123, <https://doi.org/10.1016/j.jsv.2017.06.004>.
- [47] C.Y. Sun, J.C. Hsu, T.T. Wu, Resonant slow modes in phononic crystal plates with periodic membranes, *Appl. Phys. Lett.* 97 (031902) (2010) 1–3, <https://doi.org/10.1063/1.3464955>.
- [48] M. Oudich, M. Senesi, M.B. Assouar, M. Ruzenne, J.H. Sun, B. Vincent, Z. Hou, T.T. Wu, Experimental evidence of locally resonant sonic band gap in two-dimensional phononic stubbed plates, *Phys. Rev. B* 84 (165136) (2011) 1–6, <https://doi.org/10.1103/PhysRevB.84.165136>.
- [49] Y. Xiao, J. Wen, X. Wen, Flexural wave band gaps in locally resonant thin plates with periodically attached spring-mass resonators, *J. Phys. D: Appl. Phys.* 45 (19) (2012) 1–12, <https://doi.org/10.1088/0022-3727/45/19/195401>.
- [50] C.C. Claeys, K. Vergote, P. Sas, W. Desmet, On the potential of tuned resonators to obtain low-frequency vibrational stop bands in periodic panels, *J. Sound Vib.* 332 (2013) 1418–1436, <https://doi.org/10.1016/j.jsv.2012.09.047>.
- [51] D. Torrent, D. Mayou, J. Sánchez-Dehesa, Elastic analog of graphene: dirac cones and edge states for flexural waves in thin plates, *Phys. Rev. B* 87 (115143) (2013) 1–8, <https://doi.org/10.1103/PhysRevB.87.115143>.
- [52] H. Peng, P.F. Pai, H. Deng, Acoustic multi-stopband metamaterial plates design for broadband elastic wave absorption and vibration suppression, *Int. J. Mech. Sci.* 103 (2015) 104–114, <https://doi.org/10.1016/j.ijmecsci.2015.08.024>.
- [53] Y. Song, L. Feng, J. Wen, D. Yu, X. Wen, Analysis and enhancement of flexural wave stop bands in 2D periodic plates, *Phys. Lett. A* 379 (2015) 1449–1456, <https://doi.org/10.1016/j.physleta.2015.01.037>.
- [54] E.J.P. Miranda Jr., J.M.C. Dos Santos, Flexural wave band gaps in elastic metamaterial thin plate, in: *Proceedings of the IX Mechanical Engineering Brazilian Congress (CONEM2016), Fortaleza, Brazil, 2016*, pp. 1–10.
- [55] R.K. Pal, M. Ruzzene, Edge waves in plates with resonators: an elastic analogue of the quantum valley Hall effect, *New J. Phys.* 19 (025001) (2017) 517–528, <https://doi.org/10.1088/1367-2630/aa56a2>.
- [56] S.G. Haslinger, N.V. Movchan, A.B. Movchan, I.S. Jones, R.V. Craster, Controlling flexural waves in semi-infinite platonic crystals with resonator-type scatterers, *Q. J. Mech. Appl. Math.* 70 (2017) 216–247, <https://doi.org/10.1093/qjmam/hbx005>.
- [57] O. Thorp, M. Ruzzene, A. Baz, Attenuation of wave propagation in fluid-loaded shells with periodic shunted piezoelectric rings, *Smart Mater. Struct.* 14 (2005) 594–604, <https://doi.org/10.1088/0964-1726/14/4/018>.
- [58] G.L. Huang, C.T. Sun, Band gaps in a multiresonator acoustic metamaterial, *J. Vib. Acoust.* 132 (3) (2010) 1–6, <https://doi.org/10.1115/1.4000784>.
- [59] P.F. Pai, Metamaterial-based broadband elastic wave absorber, *J. Intell. Mater. Syst. Struct.* 21 (5) (2010) 517–528, <https://doi.org/10.1177/1045389X09359436>.
- [60] H.J. Xiang, Z.F. Shi, Y.L. Mo, Periodic materials-based vibration attenuation in layered foundations: Experimental validation, *Smart Mater. Struct.* 21 (112003) (2012) 1–10, <https://doi.org/10.1088/0964-1726/21/11/112003>.
- [61] H. Shen, J. Wen, D. Yu, M. Asgari, X. Wen, Control of sound and vibration of fluid-filled cylindrical shells via periodic design and active control, *J. Sound Vib.* 332 (2013) 4193–4209, <https://doi.org/10.1016/j.jsv.2013.03.007>.
- [62] G. Kirchhoff, Über das gleichgewicht und die bewegung einer elastischen scheibe, *Journal für die reine und angewandte Mathematik* 40 (1850) 51–88.
- [63] A.E.H. Love, The small free vibrations and deformation of a thin elastic shell, *Philos. Trans. R. Soc.* 179 (1888) 491–546.
- [64] Y.C. Hsue, T.J. Yang, Contour of the attenuated length of an evanescent wave at constant frequency within a band gap of photonic crystal, *Solid State Commun.* 129 (2004) 475–478, <https://doi.org/10.1016/j.ssc.2003.11.023>.
- [65] Y.C. Hsue, T.J. Yang, Applying a modified plane-wave expansion method to the calculations of transmittivity and reflectivity of a semi-infinite photonic crystal, *Phys. Rev. E* 70 (016706) (2004) 1–6, <https://doi.org/10.1103/PhysRevE.70.016706>.
- [66] Y.C. Hsue, A.J. Freeman, Extended plane-wave expansion method in three-dimensional anisotropic photonic crystals, *Phys. Rev. B* 72 (195118) (2005) 1–10, <https://doi.org/10.1103/PhysRevB.72.195118>.
- [67] V. Laude, Y. Achoui, S. Benhabane, A. Khelif, Evanescent Bloch waves and the complex band structure of phononic crystals, *Phys. Rev. B* 80 (092301) (2009) 1–4, <https://doi.org/10.1103/PhysRevB.80.092301>.
- [68] V. Romero-García, J.V. Sánchez-Pérez, S. Castiñeira-Ibáñez, L.M. García-Raffi, Evidences of evanescent bloch waves in phononic crystals, *Appl. Phys. Lett.* 96 (124102) (2010) 1–3, <https://doi.org/10.1063/1.3367739>.
- [69] V. Romero-García, J.V. Sánchez-Pérez, L.M. García-Raffi, Evanescent modes in sonic crystals: complex dispersion relation and supercell approximation, *J. Appl. Phys.* 108 (044907) (2010) 1–6, <https://doi.org/10.1063/1.3466988>.
- [70] V. Romero-García, J.V. Sánchez-Pérez, L.M. García-Raffi, Propagating and evanescent properties of double-point defects in sonic crystals, *New J. Phys.* 12 (083024) (2010) 1–14, <https://doi.org/10.1088/1367-2630/12/8/083024>.
- [71] L. Brillouin, *Wave Propagation in Periodic Structures*, Dover Publications, New York, 1946.
- [72] G. Floquet, Sur les équations différentielles linéaires à coefficients périodiques, *Annales scientifiques de l'École Normale Supérieure* 12 (1883) 47–88.
- [73] F. Bloch, Sur die quantenmechanik der electron in kristallgittern, *Z. Phys.* 52 (1928) 555–600.
- [74] J.-M. Mencik, On the low- and mid-frequency forced response of elastic structures using wave finite elements with one-dimensional propagation, *Comput. Struct.* 88 (2010) 674–689, <https://doi.org/10.1016/j.compstruc.2010.02.006>.

- [75] K.H. Matlack, A. Bauhofer, S. Krdel, A. Palermo, C. Daraio, Composite 3D-printed metastructures for low-frequency and broadband vibration absorption, *PNAS* 113 (30) (2016) 8386–8390, <https://doi.org/10.1073/pnas.1600171113>.
- [76] A.O. Krushynska, F. Bosia, M. Miniaci, N.M. Pugno, Spider web-structured labyrinthine acoustic metamaterials for low-frequency sound control, *New J. Phys.* 19 (105001) (2017) 1–12, <https://doi.org/10.1088/1367-2630/aa83f3>.
- [77] V. Romero-García, L.M. Garcia-Raffi, J.V. Sánchez-Pérez, Evanescent waves and deaf bands in sonic crystals, *AIP Adv.* 1 (041601) (2011) 1–9, <https://doi.org/10.1063/1.3675801>.